A&A 545, A140 (2012)
DOI: 10.1051/0004-6361/201219775

Astronomy & Astrophysics

Hot gas in groups: NGC 5328 and the intriguing case of NGC 4756 with *XMM-Newton*⋆,⋆⋆

G. Trinchieri[1], A. Marino[2], P. Mazzei[3], R. Rampazzo[3], and A. Wolter[1]

[1] INAF – Osservatorio Astronomico di Brera, via Brera 28, 20121 Milano, Italy
e-mail: [ginevra.trinchieri;anna.wolter]@brera.inaf.it
[2] Dipartimento di Fisica e Astronomia G. Galilei, Università di Padova, vicolo dell'Osservatorio 3, 35122 Padova, Italy
e-mail: antonietta.marino@oapd.inaf.it
[3] INAF – Osservatorio Astronomico di Padova, Vicolo dell'Osservatorio 5, 35122 Padova, Italy
e-mail: [paola.mazzei;roberto.rampazzo]@oapd.inaf.it

Received 8 June 2012 / Accepted 26 July 2012

ABSTRACT

Context. Environment appears to have a strong influence on the fundamental properties of galaxies, modifying both their morphologies and their star formation histories. Similarly, galaxies play a role in determining the properties of the hot intergalactic medium in groups, heating and enriching it through a variety of mechanisms. NGC 5238 and NGC 4756 are the brightest unperturbed elliptical galaxies in their respective loose groups, but the analysis of their environment suggests that they may be at different evolutionary stages.
Aims. We aim to characterize the properties of the hot gas in both the halos of the brightest galaxy members and in the environment. In NGC 4756, we are also interested in the properties of a substructure identified to the southwest and the region connecting the two structures, to search for a physical connection between the two. However, we have to take into account that the group is projected against the bright, X-ray emitting cluster A1361, which heavily contaminates and confuses the emission from the foreground structure.
Methods. We present *XMM-Newton* observations of the groups and a careful analysis to separate different components. We examine the X-ray morphology, hot gas distribution, and spectral characteristics of both NGC 4756 and NGC 5328 and their companion galaxies. To better characterize the environment, we also present a re-evaluation of the dynamical properties of the systems. Smoothed particle hydrodynamical simulations are used to interpret the results.
Results. We find that the X-ray source associated with NGC 4756 indeed sits on top of extended emission from the background cluster A1361, but can be distinguished relatively well from it as a significant excess out to $r \sim 150''$ (~40 kpc). NGC 4756 has an X-ray luminosity of $L_x \sim 10^{41}$ erg s^{-1} due to hot gas, with an average temperature of $kT \sim 0.7$ keV. We measure a faint diffuse emission in the region of the subclump to the SW, but more interestingly, we detect gas between the two structures, indicating a possible physical connection. The X-ray emission from NGC 5328 is clearly peaked on the galaxy, has $L_x \sim 10^{41}$ erg s^{-1}, and extends to $r \sim 110$ kpc. Simulations provide an excellent reproduction of the spectral energy distribution and the global properties of both galaxies, which are caught at two different epochs of the same evolutionary process, with NGC 5328 ~ 2.5 Gyr younger than NGC 4756.

Key words. galaxies: elliptical and lenticular, cD – galaxies: groups: general – galaxies: groups: individual: NGC 5328 – galaxies: groups: individual: NGC 4756 – X-rays: galaxies – X-rays: ISM

1. Introduction

Observationally, we see that a large fraction (~50–60%) of the galaxies in the local Universe is in groups. These could either be isolated systems, or parts of filaments or chains, that are near to or infalling into clusters (see e.g. Eke et al. 2004; Tago et al. 2008). Groups, for which the galaxy velocity dispersion is comparable to the internal velocities of the galaxies, provide a controlled environment in which interactions (mergers) act to modify galaxy properties, for example by removing the gas that fuels star formation. Recent surveys have indeed verified that the transformation from star-forming systems into "passive" ones (Bai et al. 2010, and references therein) is a result of the environmental action over the past eight billion years, since redshift $z \sim 1$ (Kovaĉ et al. 2010; Peng et al. 2010). Cosmological hydrodynamical simulations by e.g. Kobayashi et al. (2005) and Feldmann et al. (2010, 2011) that study the evolution of groups suggest that the star-forming massive galaxies at the center of group-type potentials at $z \gg 1$ can become the massive, gas-poor early-type systems observed at the center of groups today.

We can therefore expect that the galaxies we observe in clusters today are likely to have experienced pre-processing in groups at some point in their history, before the group itself fell into the cluster formed within the same infalling halo. In their study of close pairs in the Sloan Digital Sky Survey (SDSS), Perez et al. (2009) found that galaxies are efficiently pre-processed by close encounters and mergers while in intermediate-density environments. With the same mechanism of interaction between pairs, mergers have probably depleted the reservoir of galaxies in the halo while building the dominant elliptical of the group. In addition to mergers, simulations suggest that ram-pressure stripping, once thought to operate only in rich

⋆ Based on *XMM-Newton* observations (Obs. ID 0551600101 and 0401480201 P.I. G. Trinchieri).
⋆⋆ Appendix A is available in electronic form at http://www.aanda.org

environments, is active in the form of "strangulation" in groups as well. This depletes gas-rich galaxies of their hot interstellar medium (ISM) content, which is their largest gas reservoir, leaving their molecular gas content nearly intact. On a timescale of about 1 Gyr, this process leads to the quenching of star formation in gas-rich disk galaxies, transforming them into S0s (Kawata et al. 2008). Jeltema et al. (2008) interpret the evidence that the $L_K - L_X$ relation for early-type galaxies in groups is systematically below that of field objects as indirect evidence of hot gas stripped by viscous- or ram-pressure. This is supported by more direct evidence of the action of a stripping event seen in the X-ray image of the S0 galaxy NGC 6265, located ~250 kpc west (W) of the NGC 6269 group (see also Baldi et al. 2009; or Kim et al. 2008, for NGC 7619).

However, a different scenario is proposed by Berrier et al. (2009). Their simulations actually suggest that only a small fraction (30%) of galaxies today in clusters may have been accreted from groups, while the majority have been accreted directly from the field and then reprocessed in the cluster environment.

To better understand the processes related to galaxy evolution in different environments, a careful analysis of the dynamics and the characteristics of galaxies in groups in the local Universe provides the observational data necessary to interpret the different scenarios proposed.

Tully (2010) shows that evolved groups, which are characterized by a high fraction of elliptical galaxies, have at least one dominant E galaxy and relatively few intermediate-luminosity galaxies than pristine spiral-rich groups (see e.g. Grützbauch et al. 2009). The evolution of massive ellipticals at the centers of groups, and the evolution of their hot gas content are beginning to be clarified through self-consistent models (Bettoni et al. 2012).

In this context, we adopt a multiwavelength approach to studying groups (and their members) characterized by different observational properties (e.g., galaxy density and composition, dynamical properties) to understand whether these are representative of different evolutionary stages or different evolutionary paths. We obtained data at several wavelengths through infrared (IR), optical, and ultraviolet (UV) observations with e.g., GALEX and *Spitzer* (Marino et al. 2010; Bettoni et al. 2011; Annibali et al. 2011; Marino et al. 2012; Panuzzo et al. 2011). Here we present the results of *XMM-Newton* observations of two bright early-type galaxies in poor groups, NGC 4756 and NGC 5328, which we requested in order to study the properties of the hot gas in both the galaxies and the groups. Both groups should represent relatively late evolved stages, in which an elliptical galaxy is the dominant, central member.

The hot gas in the central elliptical should result from both stellar evolution (e.g. mass loss from evolved stars) and the environment (Mathews 1990; Mathews & Brighenti 2003), and therefore is expected to be influenced by both the internal and the environmental properties of the galaxy. Evolved groups with a dominant early-type galaxy at their core typically show hot ($\sim 10^7$ K) halos detected in X-rays (see e.g. Mulchaey 2000; Mulchaey et al. 2003), but not all the details of the hot gas properties are clear at the present time.

We complement the X-ray data with a revision of the dynamical properties of the groups, and a set of smoothed particle hydrodynamics (SPH) simulations that include chemo-photometric models. These simulations provide us with predictions for the properties of the system, in particular those of the stellar population at different stages of evolution, to be compared with the observed spectral energy distribution (SED), and the hot gas (i.e. luminosity, mass...).

2. Characterization of the environments of NGC 4756 and NGC 5328

NGC 4756 is the brightest unperturbed elliptical galaxy in a loose group. The structure of the group is filamentary and complex, extending for about half a degree. The central part of the group contains a significant fraction of early-type galaxies. At about 7′ southwest (SW) of NGC 4756, a compact, Hickson-type, clump of galaxies with signatures of recent interaction has been identified (Grützbauch et al. 2005a). The NGC 5328 group, dominated by an old (12.4 ± 3.7 Gyr, Annibali et al. 2007) elliptical galaxy, has the characteristics of an evolved group (Grützbauch et al. 2005b) and is at the same distance as the Abell 3574 cluster of galaxies, as we explain below.

Both NGC 4756 and NGC 5328 and the groups associated with them were extensively studied by Grützbauch et al. (2005a) and Grützbauch et al. (2005b). However, prior to the observations presented here, inadequate X-ray data were available for both galaxies. An unpublished snapshot Chandra observation shows emission at the position of NGC 5328, which we later use to determine the presence of a point source at the center of this galaxy (see Sect. 3.1.2). NGC 4756 was observed by Einstein, the ROSAT HRI and ASCA. A strong emission peaked on the galaxy was detected in all observations. An extension to the north (N) and emission from MCG-2-33-38, a Seyfert galaxy in the SW sub-group, were also observed. In spite of the limited quality of the available data, the comparison of adaptively smoothed images from ASCA in two energy bands showed an intriguing feature that prompted us to ask for higher quality X-ray data. The soft (1–2 keV) and hard (2–8 keV) energy-band images from ASCA suggest the presence of two separate components, with different spatial distributions: a soft peak, consistent with the hot intergalactic medium associated with NGC 4756, and a hard-band centroid to the N, which is roughly at the position of a concentration of galaxies in Abell 1631 (see Grützbauch et al. 2005a).

Using the much larger spectral and photometric datasets now available in the literature, we first better characterize their environmental properties as follows.

The group around NGC 4756 is well defined in redshift space (see Fig. 1, top-left). The NASA/IPAC Extragalactic Database (NED) lists 38 galaxies with recessional velocities of 3500–4900 km s^{-1}. Of these, 29 are also listed in the HYPERLEDA database, which provides us with a uniform value of the B magnitude for 27 galaxies needed to derive the dynamical properties of the group. We therefore consider only this subset. One of the objects is PGC043424 (MCG-3-33-17), a bright spiral separated by ≈0.7 Mpc from NGC 4756 but with a similar recession velocity. Garcia (1993) had included it in the group, but its membership was revised by Giuricin et al. (2000) and Mahdavi & Geller (2001), who attributed it to a different group. We therefore consider 26 member galaxies, for which we calculate a velocity dispersion $\sigma = 460$ km s^{-1} at a mean recession velocity of 4200 km s^{-1} for the group.

Unfortunately, the group is seen projected onto the background cluster A1361 (the structure seen at ~13 000 km s^{-1} in Fig. 1, see Fig. 2), so that the spatial separation of the two structures on the plane of the sky is non-trivial. This complicates the analysis and interpretation of the X-ray data (Sect. 3.1.1).

For NGC 5238, we spatially identified a structure composed of 17 galaxies within a radius of ~700 kpc, with a velocity dispersion of 174 km s^{-1} at a mean velocity of 4755 km s^{-1} (Fig. 3). This is located at a projected distance of about 2.5 Mpc northeast (NE) of the center of the Abell 3574 cluster

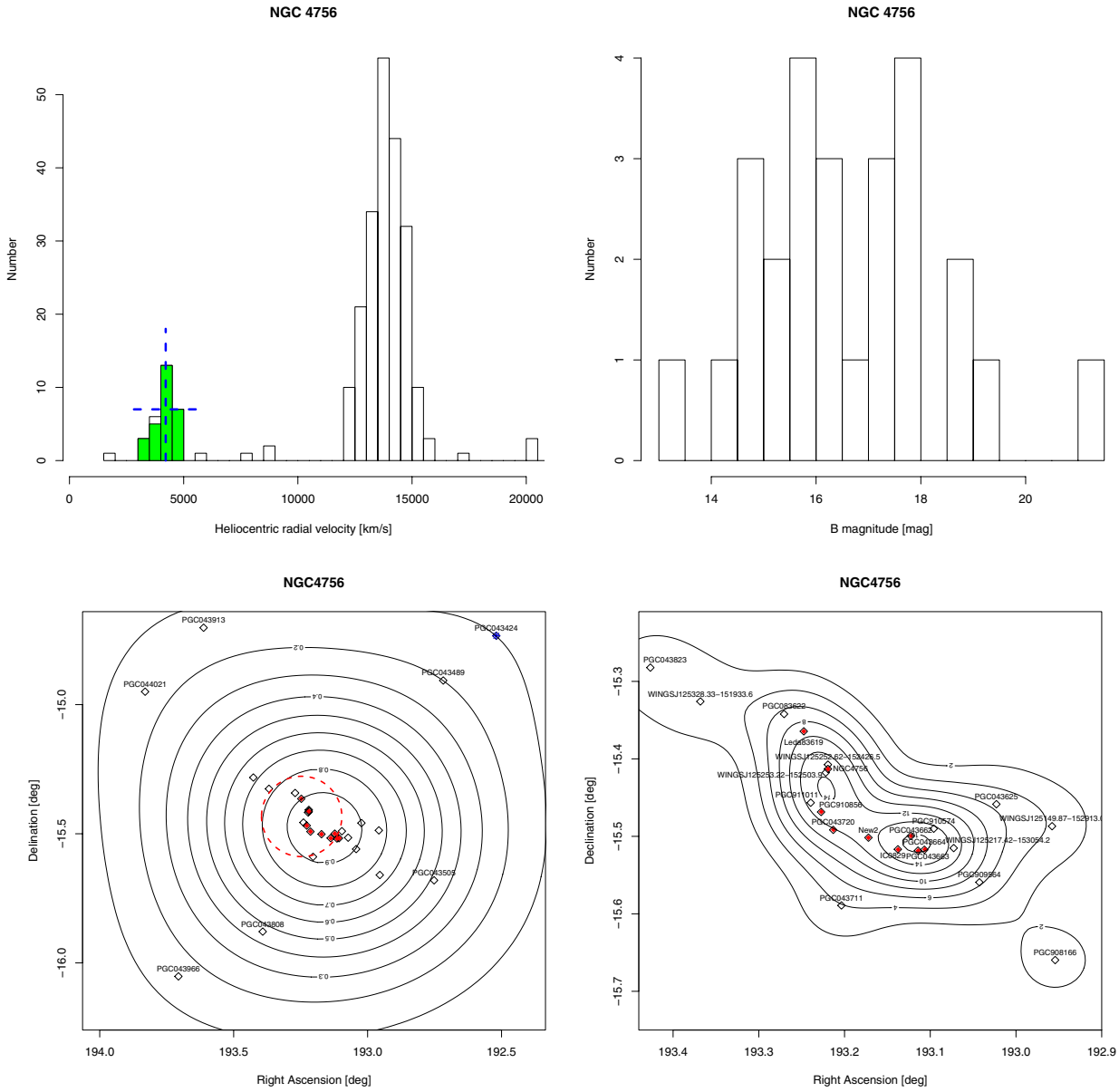

Fig. 1. *Top left*: heliocentric radial velocities in a 1.5 Mpc box centered on NGC 4756. The mean heliocentric radial velocity and the 3σ velocity dispersion of the group are identified (dashed lines). The second peak is due to A1631. *Top right*: *B* magnitude distribution of the group members. *Bottom panels*: spatial distribution of galaxies centered on NGC 4756 within 1.5 Mpc, and a zoom corresponding to the *XMM-Newton* field of view (*right*), superposed on the two-dimensional binned kernel-smoothed number-density contours. Filled red squares are group members listed in Grützbauch et al. (2005a). The dashed circle is centered on the center of mass of the group and identifies the virial radius.

(see Grützbauch et al. 2005b). Given this distance, the group cannot be considered a cluster substructure at the present time, but the continuity in redshift space between the cluster (cz = 4797 km s^{-1}) and the group suggests that the two could be connected. The group of NGC 5328 thus appears particularly suited to investigating processes occurring in galaxy groups that are likely to be accreted by galaxy clusters.

In Figs. 1 and 3, we also show the distributions of the *B* magnitudes of the member galaxies of both groups. We note that while the central galaxies NGC 4756 and NGC 5328 are equally bright, the second-brightest members differ by 1.08 and 1.81 mag, respectively. Groups with $\Delta m > 2$ mag between the brightest and second-brightest members and very luminous in X-ray emission ($L_X > 10^{42}$ erg s^{-1}) are considered evolved ("fossil") groups. The optical properties, in particular the large Δm observed between the first and second ranked members, would then suggest that the NGC 5328 could be evolved, with properties approaching those of fossil groups.

The spatial distribution of the member galaxies in the 1.5 Mpc region centered on the brighter member of each group is compared to a two-dimensional binned kernel-smoothed number density distribution of galaxies (contours) in the bottom panels of Figs. 1 and 3 for both groups. A zoomed image of the inner structure of the group corresponding to the field covered by *XMM-Newton* is also shown.

The inner, elongated (at position angle PA ≈ 57° NE) density distribution around NGC 4756 has two cusps, one in the proximity of the galaxy itself, the other generated by a compact group about 7′ SW of NGC 4756, which was originally discussed by

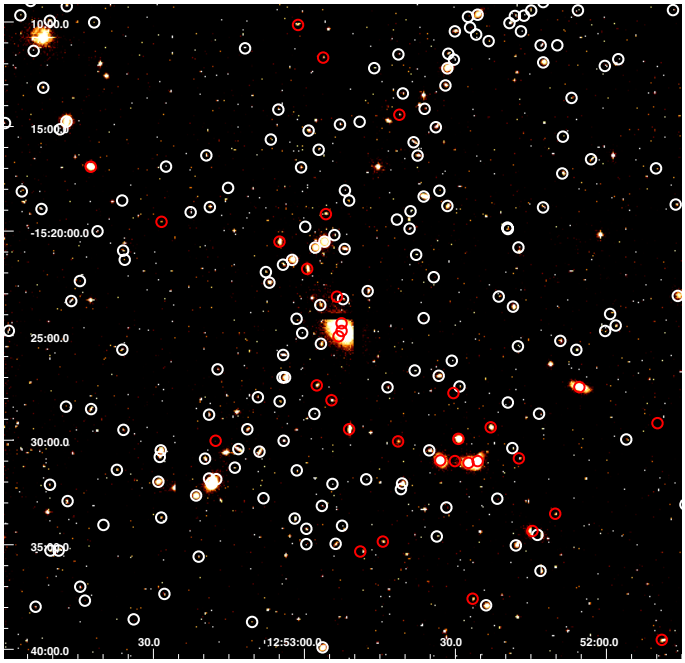

Fig. 2. Positions of the galaxies with measured velocities in the NGC 4756 field, on the un-dithered *V*-band image of Abell 1631 obtained using WFI at the 2.2-m MPG/ESO telescope at La Silla (Baade et al. 1999). Identified galaxies are at the velocity of NGC 4756 (red ~4000 km s^{-1}) or the velocity of A1631 (white, at ~13 000 km s^{-1}). Background galaxies are not labeled.

Grützbauch et al. (2005a). The inner part of NGC 5328 is composed of a chain of eight galaxies elongated along PA ≈ 61° NE.

There seems to be a sort of morphology segregation in the group of NGC 5328: among the seven brightest galaxies, two ellipticals, including NGC 5328, occupy the center of the group (in both projection and redshift space), the lenticulars are located between small and intermediate distances, and the spiral MCG-5-33-29 has the largest projected separation from NCG 5328. No elliptical galaxies are found in the outskirts of the group: the neighbouring galaxies within 1.5 Mpc are faint spiral or lenticular galaxies.

We performed a dynamical analysis of the two groups following the luminosity-weighted approach described in Bettoni et al. (2011) and Marino et al. (2010). The dynamical calculations are based on the formulae given in Table 6 in Firth et al. (2006). The results are summarized in Table 1. Each galaxy is weighted by its relative *B*-band luminosity. The coordinates of the center of mass are obtained by averaging the B luminosity-weighted coordinates of the group members.

The harmonic radii of both groups are the same and their total B luminosity comparable, but their velocity dispersions and virial masses are quite different (see Table 1, lines 1 and 3, and Figs. 1 and 3). We also computed the projected mass of both groups, which are significantly higher (close to 10×) than the virial mass. The two estimates should give similar results when the mass is distributed in a similar way to the luminosity. Heisler et al. (1985) note that the virial mass might underestimate the total mass when the more luminous galaxies are close in projection and concentrated towards the center. Projected mass estimates could be more reliable, but more sensitive to either anisotropies, subclustering, or interlopers. Discrepancies also arise if groups are in a transient configuration, i.e. accreted sub-clumps have not yet virialized. The relatively compact distribution of the galaxies in NGC 5328 might be the cause of a too low estimate of the total mass from the virial theorem. This cannot be ascribed to NGC 4756, for which galaxies are distributed over a large area. It is possible that this is instead an indication that the two subclumps have not yet reached a stable configuration. We then recomputed all quantities for NGC 4756 excluding the four galaxies in the SW clump. As shown by the results in Table 1 (line 2), the harmonic (and virial) radii are significantly different (factor of 2), the velocity dispersion is reduced by ~25% and the masses increased by a similar amount. Considering the relatively small number of objects that can be used and the complexity of the field, these estimates should be used with some caution (see also Heisler et al. 1985; Aceves & Perea 1999; Takizawa et al. 2010, for similar considerations).

3. *XMM-Newton* data

We obtained a ~28 ks *XMM-Newton* observation of NGC 5328 with EPIC instruments between January and February 2007. In December 2008, we obtained a ~70 ks *XMM-Newton* observation of NGC 4756. The EPIC detectors operated in PrimeFullWindow mode with the thin filter. We analyzed the data with the *XMM-Newton* Science Analysis Software *xmmsas*_20100423_1801 using the standard data reduction and the latest calibrations as suggested in the "User's Guide to the *XMM-Newton* Science Analysis System"[1]. We cleaned the data of periods of high flares by applying a filter to the count rate derived from the light curve provided with the standard processing (count-rates of 5 for EPIC-pn and 2 for EPIC-MOS) and obtained a clean time of 12.7 ks and 10.4 ks for EPIC-pn and for each EPIC-MOS respectively for NGC 5328 and ~24/48 ks for NGC 4756. We also identified bad pixels, bad columns, and CCD gaps, which we excluded from the analysis.

3.1. Imaging analysis

We created binned X-ray images separately for the three instruments in different energy bands for both galaxies, and a combined image from all instruments for NGC 5328 (see later and Fig. 6). Since the analysis of NGC 4756 involves non-standard procedures, and given that, unlike the case of NGC 5328, the non-operational status of one of the CCDs in EPIC-M1 heavily affected our analysis, we did not consider MOS1 data for NGC 4756. The raw images of the three instruments are shown separately in Fig. 4.

A better representation of the emission in the field is given by Fig. 5, where we have smoothed the EPIC-M2 data with an adaptive smoothing algorithm (using the task *csmooth* in the *CIAO* software, see Fruscione et al. 2006), in different energy bands. The data were uncorrected for either exposure or background at this stage, so they provided a first indication of the location of the emission, to guide the subsequent analysis. It is clear from the figure that the peak of the emission is centered on NGC 4756, but there is significant extended emission to the N and SW, and a secondary peak to the N, more evident in the harder band, at the position of two bright galaxies belonging to the cluster A1361.

For NGC 5328, we applied an adaptive smoothing algorithm with a Gaussian filter to images obtained combining the three instruments in different energy bands. The results are shown in Fig. 6 for the broad band, as a contour plot superposed on the optical Digital Sky Survey (DSS) plate. The region where the

[1] xmm.esac.esa.int/external/xmm_user_support/documentation/sas_usg/USG/

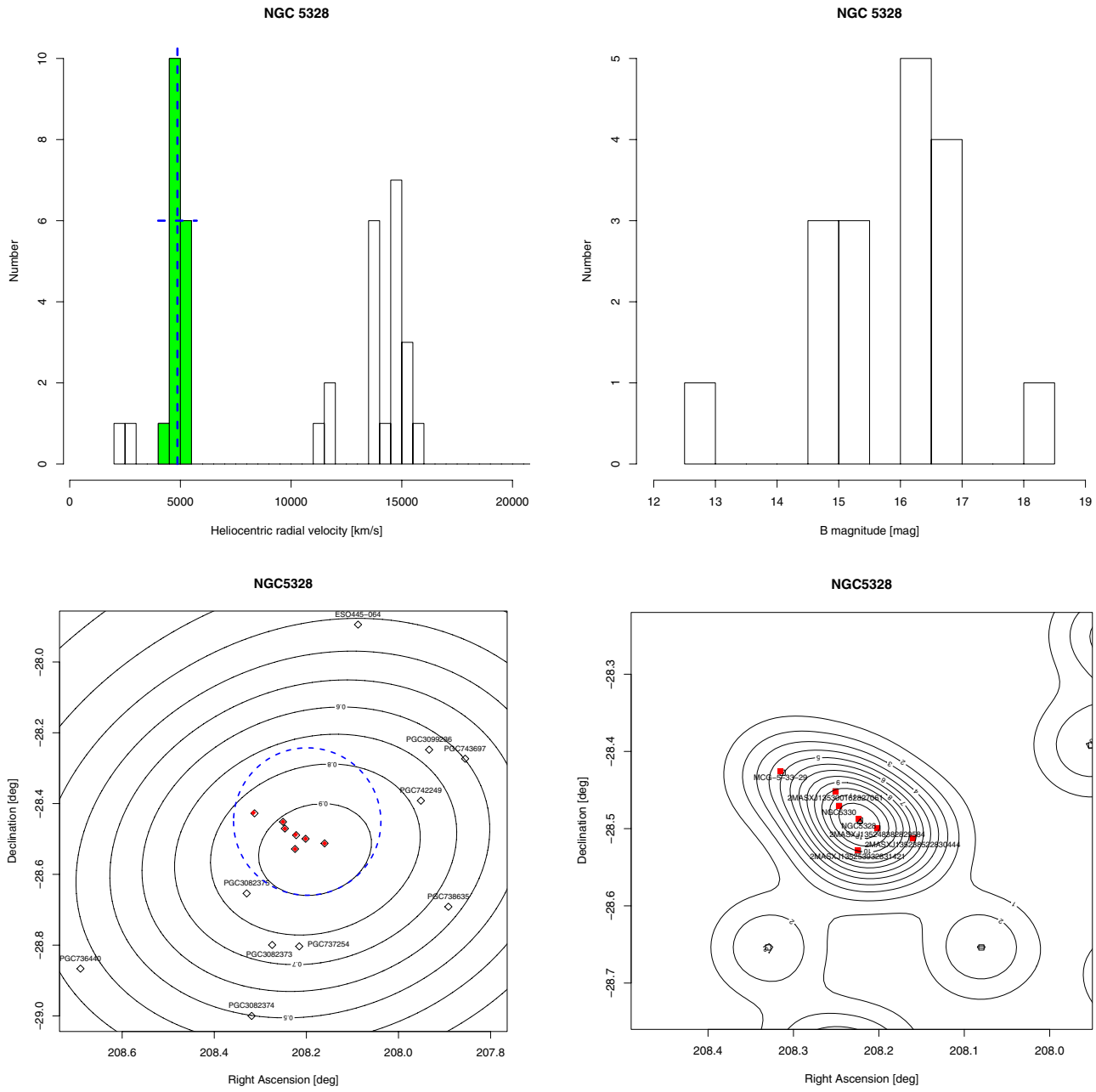

Fig. 3. Same as Fig. 1 for NGC 5328. Filled red squares are group members listed in Grützbauch et al. (2005b).

emission is detected is all within the central CCD and does not extend to the missing CCD in EPIC-MOS1.

To identify individual sources in the field of each galaxy, we ran a detection routine on the cleaned event files of the three instruments at the same time in the 0.5–4.5 keV band (see Sect. A). Besides the target, we detected a total of 68 sources in the NGC 4756 field, listed in Table A.1 and 32 in the NGC 5328 field (Table A.2). Possible identification with known objects are given.

We used these lists to identify individual sources of interest related to the target galaxies, and to exclude sources from subsequent analysis [with standard radius of 30″]. We extracted radial profiles in different energy bands and spectra in different regions together with the background, ancillary response (ARF), and detector response matrix (RMF) files for the three instruments separately, and analyzed the results with XSPEC version 12.

In what follows, we describe in more details the analysis of each target separately, since the two objects required different ad hoc procedures.

3.1.1. NGC 4756

As shown in Figs. 4 and 5, a bright source is visible towards the northern edge of the central EPIC-MOS CCD, that is coincident with NGC 4756. A few other sources are also present in the field of view: to the SW, there are a few coincident with galaxies in the southern subclump; an extension to the N coincides with galaxies belonging to the background cluster A1361.

We therefore used two different approaches for this source: we examined the data assuming the center of the emission on a) NGC 4756 and b) the secondary peak to the N, with the

Table 1. Dynamical analysis of the NGC 4756 and NGC 5328 groups

Object	N.	Center of mass		V_{group}	σGroup vel. disp.	Dist.$^{+}$	Harmonic radius	Virial mass	Projected mass	Crossing time	Group L_B
		RA	Dec	[km s^{-1}]	[km s^{-1}]	[Mpc]	[Mpc]	[10^{13} $M_\odot$]	[10^{13} $M_\odot$]	time $\times$ H_0	[10^{11} $L_\odot$]
NGC 4756	26	193.2462	–15.4330	4155.7	445	59.37	0.10	2.26	17.15	0.05	0.89
NGC 4756†	22	193.2990	–15.4006	4039.61	378	57.71	0.19	2.97	15.49	0.05	0.63
NGC 5328	17	208.1982	–28.4508	4754.88	174	67.93	0.10	0.34	2.23	0.09	1.24

Notes. All parameters are weighted by B-band luminosity using $M_{B\odot}$ = 5.45 mag. $^{(+)}$ Distance is derived from V_{hel} adopting H_0 = 70 km s^{-1} Mpc^{-1}. This gives a scale of 0.302 kpc/″ for NGC 4756 and 0.326 kpc/″ for NGC 5328. $^{(\dagger)}$ The dynamical analysis of NGC 4756 is repeated by excluding the four galaxies in the SW clump (see text).

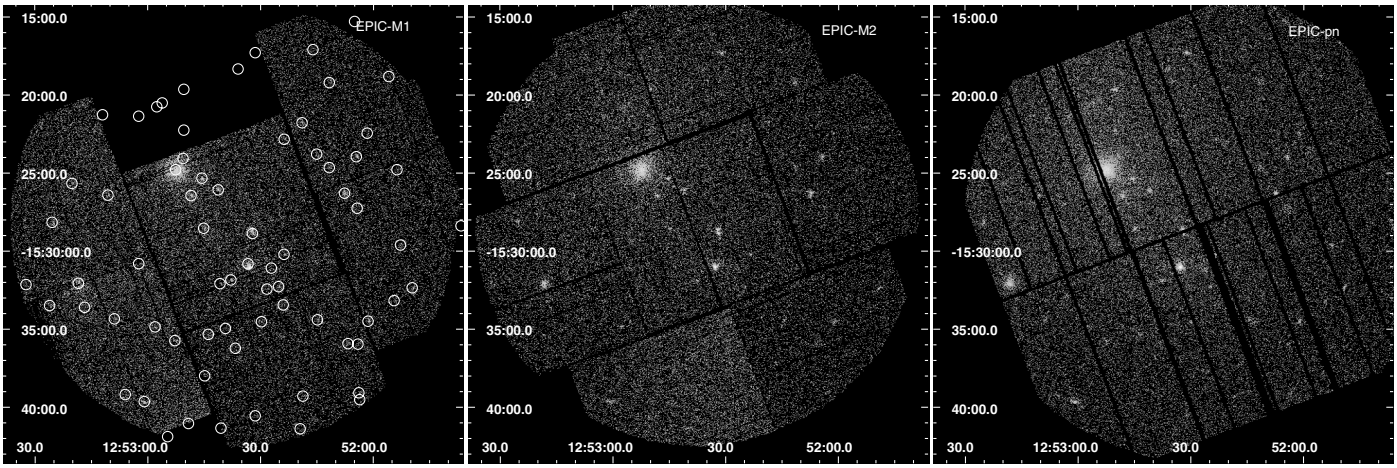

Fig. 4. *XMM-Newton* images of NGC 4756 from the three EPIC instruments. The positions of the detected sources are shown on the EPIC-M1 image.

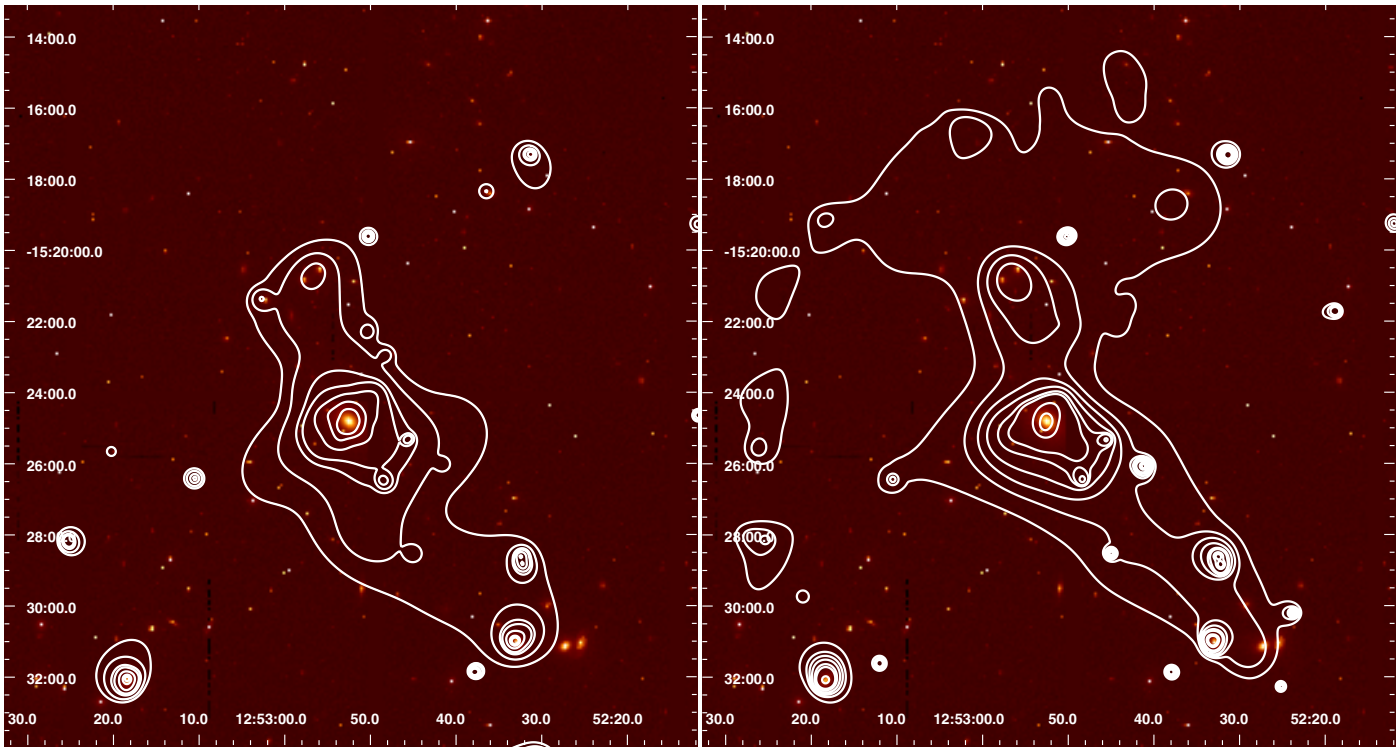

Fig. 5. Isointensity contours from the EPIC-MOS2 image treated with an adaptive smoothing algorithm (*csmooth*) in different energy bands: 0.3–1.0 keV (*left*) and 1.0–3.0 keV (*right*), superposed onto a Digital Sky Service DSS-II red plate.

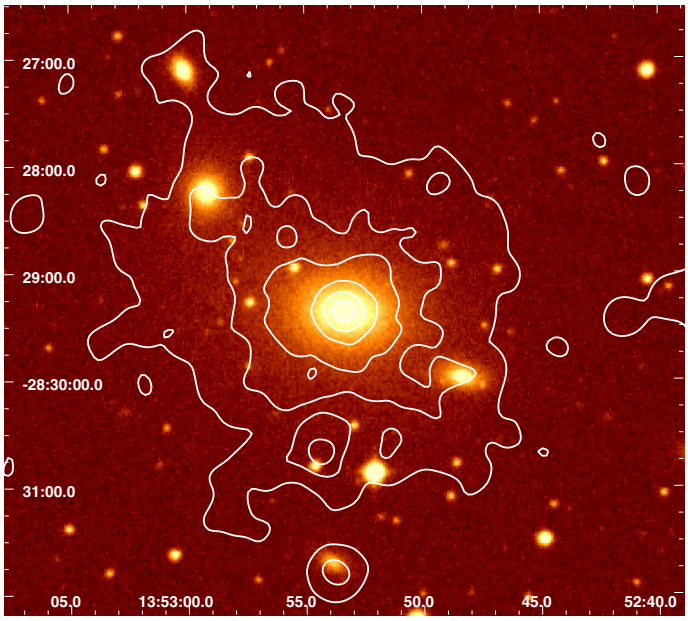

Fig. 6. X-ray iso-contours from the smoothed 0.3–7 keV image of NGC 5328 (from *csmooth*) obtained by combining all three instruments superposed onto the optical image from the DSS-II red plate.

aim of disentangling the emission from the two components – foreground group and background cluster. We report here the analysis step-by-step and summarize the results in Sect. 4. We extracted radial profiles from both EPIC-pn and EPIC-MOS centered on the peak of the emission on NGC 4756 in different bands (we show the broad-band profiles in Fig. 7), azimuthally averaged over 360°, and in different regions of the field of view. As a first approach, we extracted profiles separately for the northern and southern half of the plane in circular concentric annuli of increasing width with radius, and for the four NSEW directions.

All profiles appear to have a radial gradient out to $r \sim 600''$, with the exception of the E direction that traces a smaller range, indicative of emission above the expected background at least out to these radii. However, we need to take into account that the profiles trace very different regions of the detector, owing to the off-center position of the source. We therefore requested blank sky images appropriate for this field from the *XMM-Newton* sky background team[2], which we used to estimate the shape of the profile of the background emission in the same regions.

The selection criteria for the blank sky fields that we found most appropriate for the success of our analysis were based on revolution, column density, and spatial direction, with the additional constraint on the presence [or rather absence] of detected sources in the fields. More specifically, only fields taken with the following constraints were considered: a) only revolutions subsequent to the loss of CCD6 in EPIC-MOS1 (revolution 961 and after); b) Galactic column densities $N_{\rm H}$ in the range $1.5–4.5\times10^{20}$ cm^{-2}; c) pointings within a radius of 90° from the direction of NGC 4756; d) no more than two sources in the region between NGC 4756 and the southern sub-condensation, and none with a flux $f_{\rm X} > 6\times10^{-13}$ erg cm^{-2} s^{-1} (0.2–12.0 keV). The reference list used was the second *XMM-Newton* source catalog. The final blank fields were cleaned using the same criteria as the original files.

To normalize the blank sky fields to the data, we first rescaled the background for the relative exposures, and then applied a small correction to better match the light distributions. The correction is on the order of 10%. The resulting radial profiles are also shown in Fig. 7.

A comparison of the profiles in the northern and southern halves in different bands suggests a systematic excess best seen in the intermediate 1–3 keV energy range in the northern half at $r > 150''$. Little difference is seen between the profiles obtained in the S and W directions. We therefore refined our choices of regions, so that the N sector is included between ∼−45° and ∼70° (counterclockwise, from N), and the SW is in the range ∼140−315°.

We then produced background-subtracted profiles shown in Fig. 8 for the 0.3–1 and 1–3 keV band, obtained using the rescaled blank-sky profiles from the same regions in the same energy bins. It is evident that the level of emission is different in the two directions, higher towards the N outside $r \sim 150''$, and most evident in the 1–3 keV range. The emission extends in both directions out to the edges of the field of view.

A second difference between the profiles in the two bands is the relative importance of the central peak to the more extended emission. This can be seen from the comparison of the β-type models that we plot together with the data. We note that these are not fits to the data, although they could be representative of the emission out to radii of $250''–300''$ in the SW direction. While the overall normalization is smaller in the 1–3 keV band, relative to the 0.3–1 keV, we also had to reduce the relative normalization between the inner and outer models, by a factor of ∼1.5. This could be indicative of two distinct components, one dominating below $r \sim 50''–70''$, with different spectral characteristics. This is discussed further in Sect. 3.2.

Given the evidence of emission in all directions, and stronger to the N, we moved the center of the profiles onto A1361, to better define the contribution from the cluster. This is even further out than NGC 4756, outside the central CCD in the EPIC-MOS and close to the edge of the field. We considered different directions to derive the radial profiles, and chose the configuration shown in Fig. 9. Given the off-axis location of the cluster, we could use 360° annuli only in the innermost region, before getting too close to the edge of the field. We have then chosen a preferred direction to maximize the contrast and highlight the emission from the galaxy and group relative to that of the cluster. In Fig. 10, we present the resulting net profiles above the background that we estimated from the blank sky fields used above. We show the EPIC-M2 data, since it has fewer CCD gaps, and none between NGC 4756 and the southern subclump of interest (see later). We could not use EPIC-M1 since the cluster would fall on the lost CCD.

The profiles we obtained indicate that 1) there is a general decrease in the emission centered on A1361, which is consistent with emission from a cluster, out to a radius $r \sim 400''–600''$ in all directions we could probe; 2) the contribution from NGC 4756 is evident at radii greater than 150″, in the profile obtained in the S-SW direction; 3) the central regions of the 1–3 keV profile indicate stronger emission than in the softer band, unlike the profiles obtained for NGC 4756, indicating a rather different spectrum; 4) the softer profile shows an excess out to ∼800″ in the S-SW direction, relative to the profiles obtained in the contiguous regions, while a possible excess in the harder band is less convincing. This confirms that there is emission from the hot gas in NGC 4756 in excess of what is expected from the background cluster, and indicates that the emission extends in the direction towards MCG-02-33-038.

Two other galaxies in the NGC 4756 group were detected: IC0829 and MCG-02-33-038 in the southern sub-clump (see

[2] http://xmm.vilspa.esa.es/external/xmm_sw_cal/background

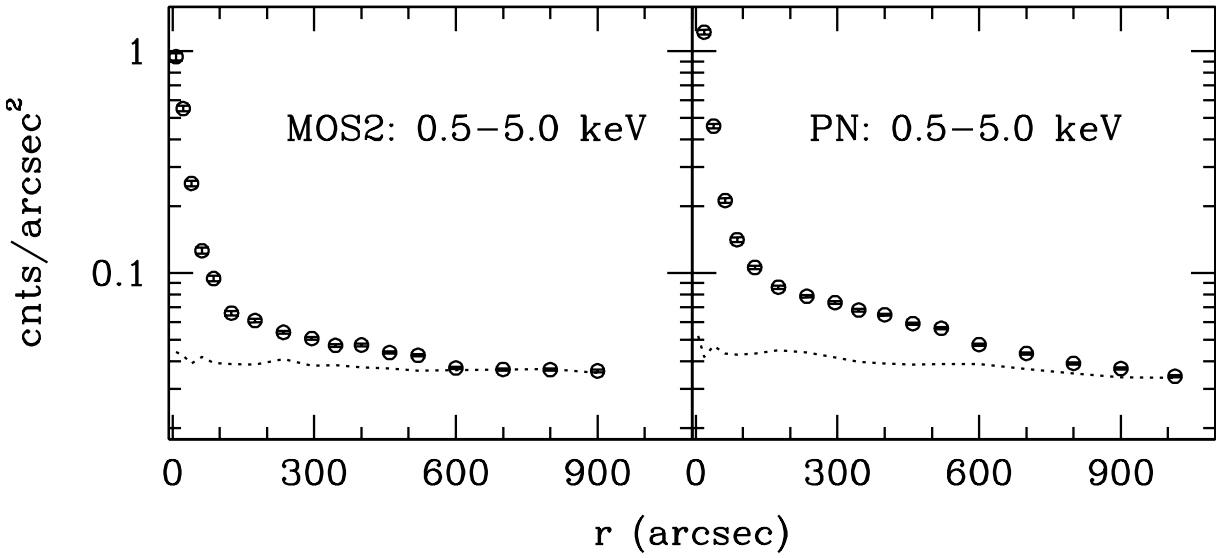

Fig. 7. Raw profiles in a broad energy bands from clean EPIC-pn and EPIC-M2 data, centered on NGC 4756, azimuthally averaged over 360°. Dashed lines: blank sky appropriately cleaned and sky-casted, produced from observations in neighbouring fields, and normalized to match the data at large radii (see text).

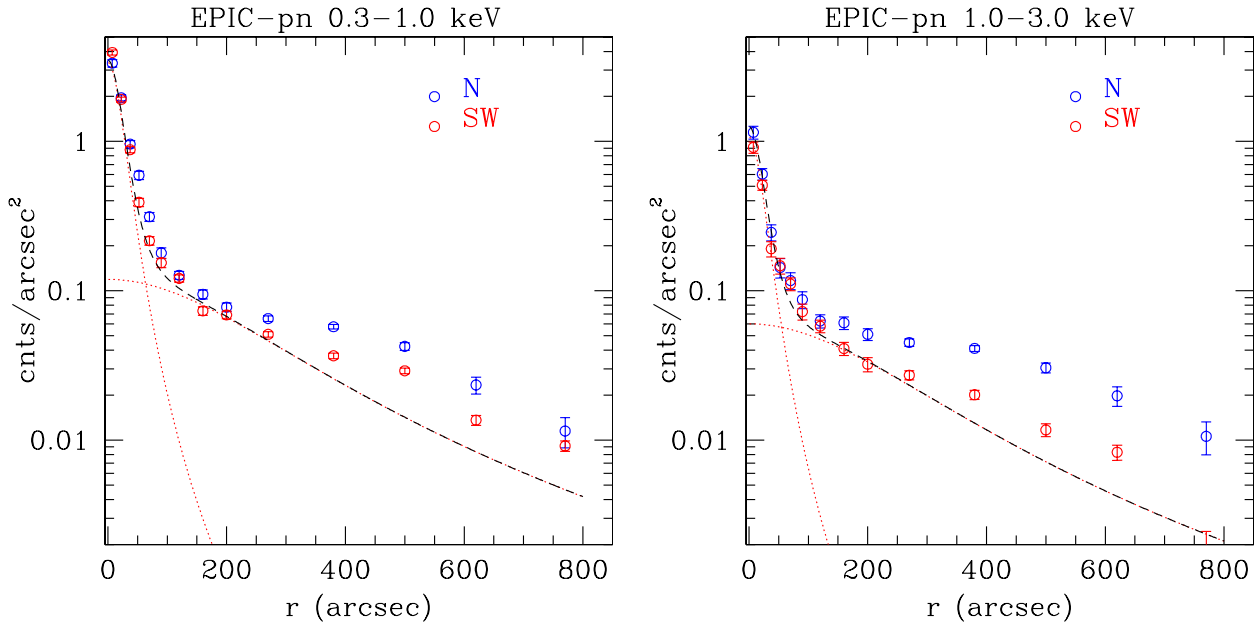

Fig. 8. Azimuthally averaged net profiles in the 0.3–1 and 1–3 keV band from clean EPIC-pn data. Center on NGC 4756, azimuthally averaged between ~315−70° (N) and ~140−315 (SW). Background is from the normalized blank sky profiles in the same region. The dashed line indicates the model composed of two β-models with $r_c = 33''$, $\beta = 0.9$ and $r_c = 300''$, $\beta = 0.7$.

Appendix and Table A.1). Table 2 summarizes the characteristics of these galaxies, together with their fluxes in a soft and a hard energy band. We re-evaluated their X-ray luminosity above a local estimate of the background, which takes into account possible local diffuse emission. We extracted the source counts from EPIC-pn in a circle of 20″ and 30″, respectively. For MCG-02-33-038, we have enough counts to fit the spectrum with a more appropriate model (a slightly absorbed power-law with $\Gamma = 2.1$, see next section), that reflects the presence of a low-luminosity nuclear source. IC0829 does not have enough counts for a spectral analysis, so we used the standard model, $\Gamma = 1.7$ and Galactic absorption, to evaluate the flux. The luminosity of IC0829 is entirely consistent with what could be expected by the low-mass X-ray binary (LMXB) population in a galaxy of the same K-band luminosity (Boroson et al. 2011).

3.1.2. NGC 5328

Figure 6 shows extended emission clearly peaked on NGC 5328. A slight elongation towards NGC 5330 to the NE is visible. NGC 5330 itself is also detected, though marginally, as confirmed by the source detection algorithm, which detects three additional members. Table 2 gives some of their basic properties, together with the net counts (with errors) from EPIC-pn, the flux, and the luminosity. Fluxes are obtained by assuming a simple spectral representation with a power law with the slope fixed at $\Gamma = 1.7$ and Galactic N_H. Luminosities are on the order of 10^{40} erg s^{-1}, which are typical of normal early type galaxies.

We extracted radial profiles from the emission of NGC 5328 using concentric annuli centered on the X-ray peak. We used the mask files and source regions produced before to exclude

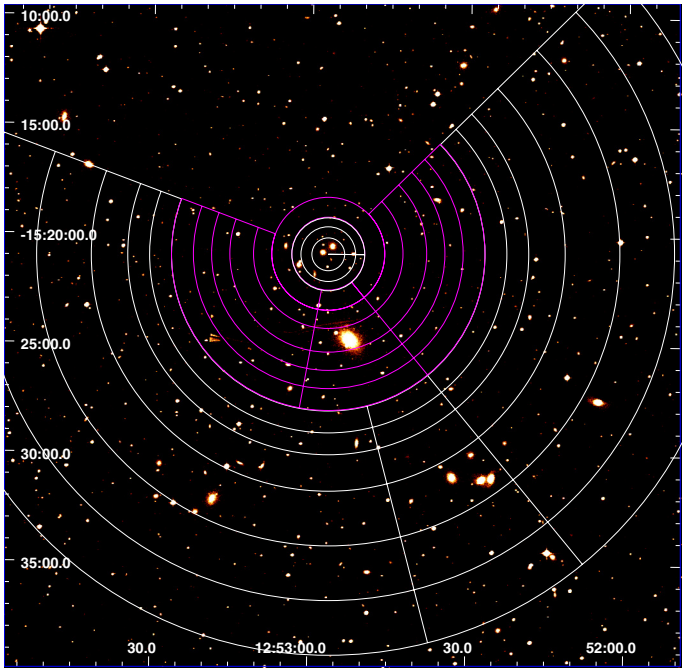

Fig. 9. Regions used to derive the radial profiles shown in Fig. 10. The annuli in the innermost region are azimuthally averaged over 360°, in the outer regions the angles are chosen both to accommodate the limits of the field of view and maximize the emission in the S direction towards MCG-02-33-038.

"dead columns", gaps, and detected sources. The radial profiles extracted from the EPIC-pn in the 0.3–2 keV and 2–7 keV bands are shown in Fig. 11.

It is immediately evident from the figure that the emission is extended in the soft band, while at harder energies the emission is limited to the innermost region, at $r < 50''$, and then becomes almost constant with radius.

To better evaluate the total extent of the source, we compared the radial profile obtained for NGC 5328 with that obtained from the *XMM-Newton* blank sky fields (see above). We extracted this latter from event files cleaned using the same procedure used for NGC 5328 data, rotated and sky-casted to match the original data, from the same region file centered at the same position. We note that the shape of the blank sky profile, arbitrarily renormalized to match the data at large radii provides a good representation of the profile for radii $r > 300''-350''$. We therefore used this radius as the maximum extent for this source. This corresponds to a physical radius of ∼100 kpc. The comparison in the hard band confirms that the emission extends only out to $r \sim 50''$.

The net profile of the emission in the 0.3–2.0 keV band is shown in Fig. 12. In the same figure, we also plot a combination of two β-type models that could represent the radial distribution of the emission (as for NGC 4756, these are not fits). In this case, a single model could represent the data with the exception of a small excess at the center, i.e. $r < 30''$.

To better understand the origin of this excess, we checked the Chandra image for the existence of a central point source. The very short exposure collected about 250 counts (0.5–2.0 keV band) in a region of 40″ radius centered on the galaxy. The radial distribution of the photons indicates that the source is extended, at least to the optical extent of the galaxy. A crude estimate of the flux based on a APEC MODEL indicates a flux that is consistent with that measured by *XMM-Newton* in the same region. It is therefore likely that the excess in the *XMM-Newton* data is due to the emission from the galaxy itself, while a group component contributes to the emission at larger radii.

3.2. Spectral analysis

We used a local background, extracted from the same datasets (rather than from the blank sky fields) in well-chosen regions appropriate for our purposes. This ensures that we indeed obtained the most representative background for each region that we study, although in some cases small corrections for different responses in different parts of the detector might be appropriate. Since the source regions are relatively compact and centrally located in NGC 5328, and given the complexity of the field around NGC 4756, we feel that these are significantly less important than any correction that would have been required had we used blank sky fields to correct for background. We present the results that we obtained using the EPIC-pn data, that had also been checked against the EPIC-MOS data in equivalent regions. We used a combination of APEC and power-law models with line-of-sight absorption at low energies (3.5 and 4.6×10^{20} cm^{-2}, Kalberla et al. 2005, for NGC 4756 and NGC 5328, respectively). For the APEC, we considered metal abundances of 50–100% the cosmic value, using the abundance tables of Anders & Grevesse (1989). To improve the statistics, we binned the spectral data. Depending on the statistics, we ensured either that we included 30–60 counts per bin or that we reached a 2σ level after background subtraction.

3.2.1. NGC 4756

The source associated with NGC 4756 is clearly projected onto more diffuse emission from the background cluster. We therefore identified a few regions where we could safely isolate NGC 4756 as the dominant component, and used the neighbouring regions, that include the cluster emission, as the background.

The X-ray peak on NGC 4756 and surrounding regions are clearly well above the expected cluster emission, so we selected a region of 45″ radius (corresponding to the major-axis size of the galaxy) and the adjacent annulus with an outer radius of 135″ (close to the maximum extent seen in Fig. 10) to characterize the emission from NGC 4756 and its immediate surroundings.

We also selected a circle of 75″ radius, with the exclusion of the Seyfert nucleus, to characterize the southern compact group, and an ellipse along the connection between NGC 4756 and the southern group (see Figs. 5 and 10) to trace the emission between these two systems.

We found that the spectrum of NGC 4756 is well-described by an APEC model with $kT \sim 0.64 \pm 0.02$ keV and $N_{\rm H} \sim 2 \times 10^{20}$ in excess of the Galactic value (but consistent within the 90% errors with the line-of-sight value), and luminosity of $\sim 1.3 \times 10^{41}$ erg s^{-1} (0.5–2.0 keV). The data do not require a power-law component, but can accommodate one with an index fixed at the value $\Gamma = 1.7$, which contributes a luminosity of $\sim 3.3 \times 10^{39}$ erg s^{-1} (0.5–2.0 keV) or $\sim 9.3 \times 10^{39}$ erg s^{-1} in the 0.3–8.0 keV band. This is actually slightly lower (but consistent within errors) than the contribution from LMXB sources estimated by Boroson et al. (2011) based on the K-band luminosity.

The surrounding region has $kT \sim 0.76 \pm 0.03$ keV, and a luminosity of $\sim 5 \times 10^{40}$ erg s^{-1} (0.5–2.0 keV). In this dataset, there is a requirement of a power-law component with $L_{\rm x} \sim 2.1 \times 10^{40}$ erg s^{-1} (0.5–8.0 keV). An equivalently good fit is obtained by using a second APEC component, with $kT \sim 3.6$ keV

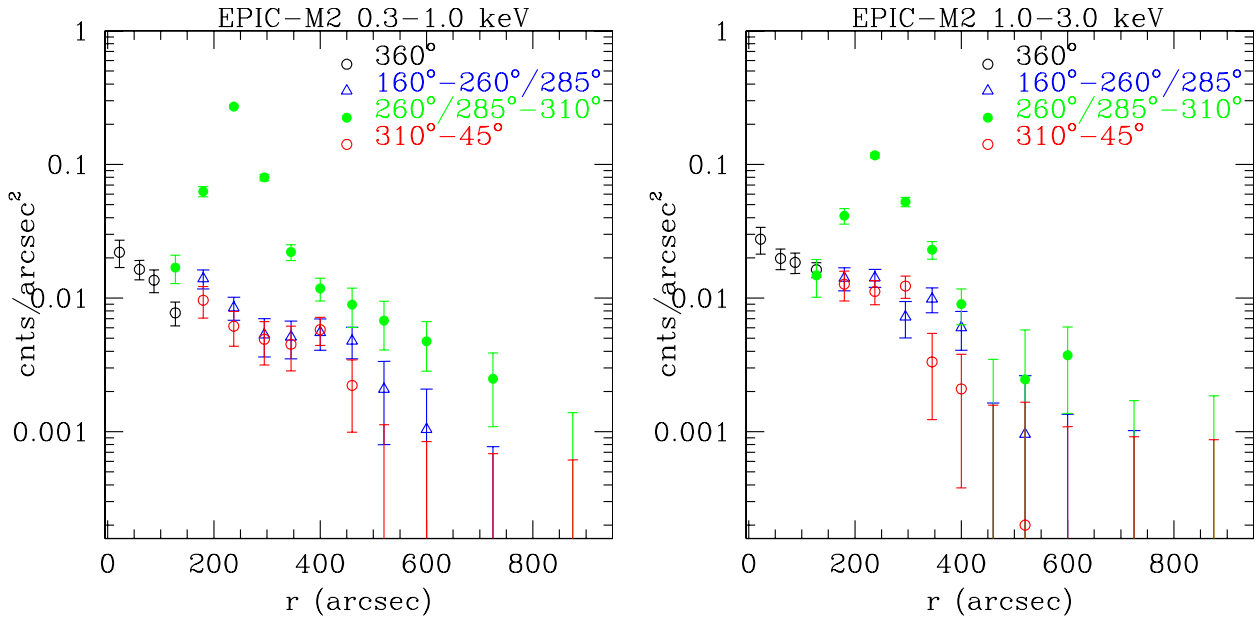

Fig. 10. Azimuthally averaged net profiles in the 1–3 keV band from clean pn data. Center on NGC 4756, azimuthally averaged over 180°. Background is from the normalized blank sky profiles in the same region. The northern half shows excess starting at ∼100″ radius.

Table 2. Detected members.

Object	Morphology	log L_b	log L_k	Radius [X rays] kpc	Net counts 0.5–4.5 keV EPIC-pn	f_x 0.5–2; 2–10 keV erg cm^{-2} s^{-1}	L_x 0.5–10 keV erg s^{-1}
			NGC 4756 group				
NGC 4756[†]	E3	10.43	11.23	40	6038.2 ± 119.8	4.8; 0.2×10^{-13}	2.1×10^{41}
IC0829	SB0	10.02	10.82	4.5	67.9 ± 11.0	4.7; 8.5×10^{-15}	5.7×10^{39}
MCG-02-33-038[†]	S0/a	9.81	10.50	9	871.0± 33.2	7.4; 7.2×10^{-14}	6.3×10^{40}
			NGC 5328 group				
NGC 5328[†]	E1	10.89	11.58	110	1906.5 ± 54.8	6.4; 0.6×10^{-13}	3.9×10^{41}
PGC3094716	E	9.57	10.35	4.9	85.3 ± 20.5	4.9; 8.9×10^{-15}	7.7×10^{39}
NGC 5330	E/E1	10.07	10.74	4.9	292.4 ± 25.0	1.7; 3.1×10^{-14}	2.6×10^{40}
2MASX J13525393-2831421	S0/SB0	9.12	9.82	4.9	77.4 ± 20.3	4.4; 8.1×10^{-15}	7.0×10^{39}
ESO 445- G 070	SB(r)0/a	9.84	10.63	4.9	30.0 ± 9.0[††]	3.3; 6.1×10^{-15}	5.2×10^{39}

Notes. Data from NED and EPIC-pn. K-band luminosities assume $M_{K\odot} = 3.28$. X-ray fluxes and luminosities are computed assuming a power law model with $\Gamma = 1.7$ and line-of-sight absorption of 3.5 and 4.6×10^{20} cm^{-2}, for NGC 4756 and NGC 5328 respectively (Kalberla et al. 2005). [(†)] X-ray quantities derive from the spectral analysis, assuming a plasma model for NGC 4756 and NGC 5328, and power law with $\Gamma = 2.1$ for MCG-02-33-038. For NGC 4756 flux and luminosities refer to the soft ($kT \sim 0.7$ keV) component only. [(††)] On a gap in EPIC-pn; counts are derived from the sum of the 2 EPIC-MOS.

($kT > 1.5$ keV) and 50% cosmic abundances. This could represent a second "group component" or some contribution from the background cluster (at $L_x \sim 1.4 \times 10^{41}$ erg s^{-1}, 0.5–2.0 keV, at the distance of the cluster).

Similar values are observed in the extended emission of the southern compact group. The mean temperature is $kT \sim 0.68$ and the luminosity is $L_x \sim 3.6 \times 10^{39}$ erg s^{-1}. We also found a slightly better minimum at $kT = 0.2$ keV, but this would also require a significantly higher absorption $N_H \sim 6 \times 10^{21}$, which is not observed in the neutral hydrogen. A power law with (fixed) $\Gamma = 1.7$ is needed to explain the high energy tail, with a contribution of $L_x \sim 6.3[10.4] \times 10^{39}$ erg s^{-1} [0.5–2; 2–10], to account for the excess at high energies. It is unlikely that this is due to the contribution of the Seyfert nucleus, which is not included in the spectral region, but has a steeper spectrum with $\Gamma = 2.1 \pm 0.2$ and moderate intrinsic absorption ($N_H \sim 4 \times 10^{20}$, $<8 \times 10^{20}$ cm^{-2} at the 90% confidence; see also Table 2).

3.2.2. NGC 5328

We extracted the X-ray spectrum of the target in a circle of radius $r = 40''$, centered on NGC 5328, and in the adjacent annulus of inner/outer radii of 40″ and 350″. The background is derived from a set of source free circles outside the extended emission.

We used an APEC model to represent the hot gas. We fixed the Galactic absorption to the line-of-sight value of $N_H \sim 4.6 \times 10^{20}$ cm^{-2}.

The temperatures in the inner and outer regions are very similar, but formally different at $kT = 0.85 \pm 0.2$ and $kT = 0.95 \pm 0.4$ (inner/outer, respectively), which is indicative of a slightly lower

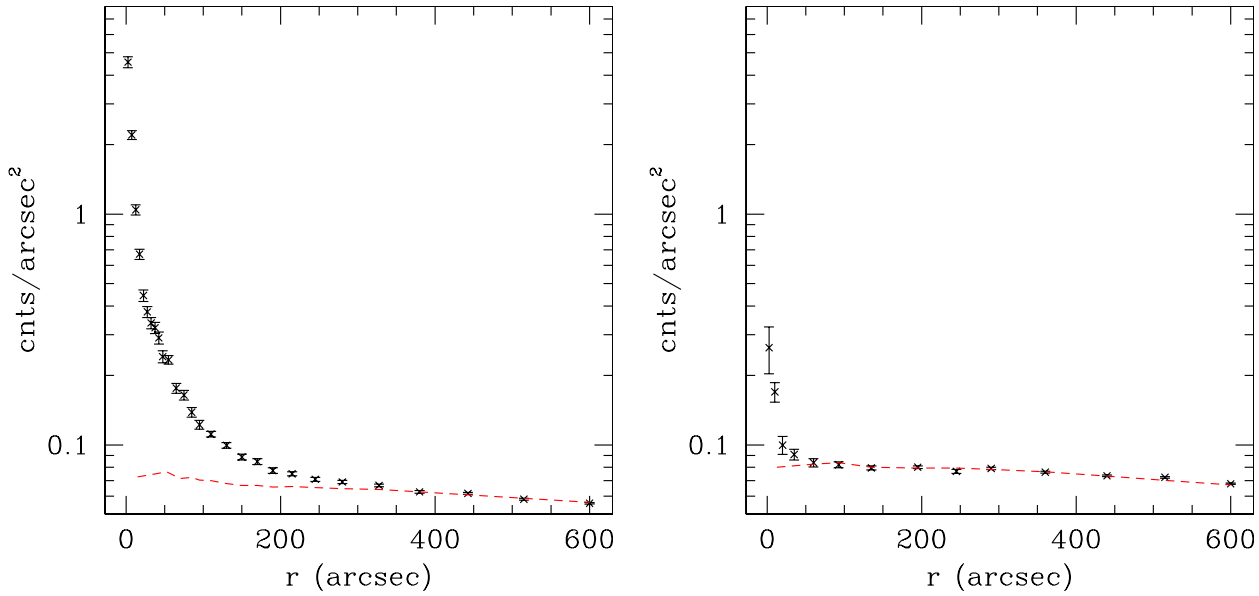

Fig. 11. Azimuthally averaged raw radial profile of the emission from NGC 5328 observed with EPIC-PN in 0.3–2 keV (*left*) and 2–7 keV (*right*) bands. The red line is the shape of the blank sky profile arbitrarily normalized to the data.

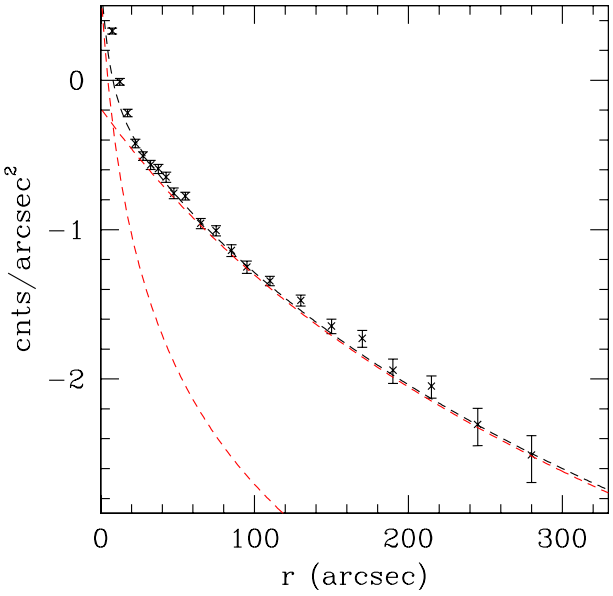

Fig. 12. Azimuthally averaged net profile of the emission from NGC 5328 observed with EPIC-PN in 0.3–2 keV. The dashed line represent a model given by the sum of two β-models with: $r_c = 6.6''$; $\beta = 0.63$ (PSF) and $r_c = 160''$; $\beta = 1.05$.

temperature towards the center. The χ^2_ν is in the range of 1.1–1.4 (for 304 d.o.f.). There is no need for the power-law contribution expected from binaries, which however is expected to be well below the plasma component. The gas has intrinsic luminosities of $L_x = 9.81 \times 10^{40}$ erg s^{-1} and $L_x = 2.56 \times 10^{41}$ erg s^{-1} (0.5–2 keV) in the inner and outer regions, respectively.

4. Results from the X-ray data

The spatial analysis of the fields of NGC 4756 and NGC 5238 indicates that both galaxies sit at the center of a large halo of hot gas. The shape of the emission around NGC 5328 suggests that it is a rather relaxed, small group of total size ~110 kpc radius and luminosity $L_x \sim 3.5 \times 10^{41}$ erg s^{-1}.

The presence of the background cluster onto which NGC 4756 is projected prevents us from determining the shape and the true extent of the emission, although we have evidence that there is a connection with the sub-group to the SW, at ~130 kpc. The luminosity that we can attribute to this system is $L_x \sim 2 \times 10^{41}$ erg s^{-1} within ~40 kpc, and $L_x \sim 10^{40}$ erg s^{-1} from the southern clump and the intermediate region. This is probably an underestimate of the total emission from this system as a whole, since we only measured the emission from selected regions, where the contamination from the background cluster can be quantified.

In both cases, a soft thermal plasma with a temperature of around 0.6–0.9 keV is detected at the center, with somewhat higher values towards the periphery, which is consistent with what is observed in other groups of galaxies (e.g. NGC 4261 O' Sullivan et al. 2011, and references therein).

A few member galaxies are detected, besides the central ones, with luminosities of about $L_x \sim 10^{40}$ erg s^{-1}, in line with the X-ray luminosities of the LMXB component in normal, early-type galaxies of that optical/IR luminosity. A higher luminosity $L_x \sim 6 \times 10^{40}$ erg s^{-1} is observed in MCG-02-33-038, to the SW of NGC 4756, which can be attributed to a slightly absorbed Sey2 nucleus. The other Sey2 nucleus, ESO445-G070 [MCG-5-33-29] in the NGC 5328 group, has a lower luminosity than MCG-02-33-038, but marginally higher than expected from the LMXB contribution in early-type galaxies (Boroson et al. 2011). NGC 5330 is detected with a luminosity of $>10^{40}$ erg s^{-1}. This galaxy is embedded in the large scale emission and $<2'$ from NGC 5328. It is detected with too few counts for a proper spectral investigation and for a separation from the overall diffuse emission, which could contribute to the value we found, although we cannot exclude that the relatively high value of the luminosity is due to a small contribution from a nucleus, or a small gaseous component in the galaxy.

Within the limitations of current statistics, we lack evidence of a gaseous component in the detected members of either groups. This differs from what Jeltema et al. (2008) found in their analysis of 13 nearby groups, where they detected emission from gas in a large fraction of the objects, although with lower luminosity than in field systems of the same *K*-band

luminosity. Jeltema et al. (2008) interpreted this as a result of mild ram pressure, which acts on the galaxies although less efficiently than in clusters. Taken at face value, this result would suggest that stripping has been even more efficient in these two groups than in the 13 studied by Jeltema. The luminosities of the extended emissions in NGC 4756 and NGC 5328 are comparable to relatively faint systems in Jeltema, such as HCG 42 and NGC 3557, which also have comparable or higher velocity dispersions (~300 km s^{-1}), so we could expect a similar action from the ambient medium. Three objects were detected in NGC 3557 at luminosities $L_{\rm x,gas} \sim 4$–40×10^{39} erg s^{-1} (0.5–2.0 keV), while no detections were found in HCG42, with limits at $L_{\rm x,gas} \simeq 1 \times 10^{39}$ erg s^{-1}. The higher spatial resolution of the Chandra data used by Jeltema could contribute to their higher success in measuring hot gas. However, the K-band luminosities of the galaxies in NGC 4756 and NGC 5328 are lower than those of the detected galaxies in Jeltema (see their Fig. 1), so we cannot exclude that our failure to detected hot gas in them is due to the significantly lower values expected.

We note that the X-ray luminosities that we detect are relatively low for groups, but consistent with the tail end of the distribution. If we attribute all of the luminosity to the central galaxy, the area covered by the detected emission is significantly larger than that of the stellar light, so it is reasonable to expect a contribution from a more massive potential. If we were to assume that the inner region studied in the spectral analysis and roughly identified with the inner β-model component (see Figs. 8 and 12) corresponds to the galaxy proper, then the emission would be co-spatial with the stellar light ($\leq D_{25}$). This is also consistent with the [marginal] evidence that the inner region is softer, and may be due to a sizable contribution from the gas produced by stellar sources and retained within the optical extent of the galaxy.

5. Modeling

The optical, X-ray, and spectroscopic observations provided us with different pictures of the two groups. NGC 5328 is at the center of its group, while NGC 4756 is located on the NE side. At about 7′ SW of NGC 4756, a dense agglomerate of galaxies, identified by Grützbauch et al. (2005a) as a Hickson-like compact group, is likely evolving as a substructure, contributing <20% of the total mass. The analysis of the velocities of group members showed that the velocity dispersions differ by about a factor of two (larger in NGC 4756), while the harmonic radii are the same.

Within the limitations imposed by the complexity of the NGC 4756 field, the X-ray luminosities of NGC 4756 and NGC 5328 are comparable, while the large-scale spatial distributions were difficult to compare. The indication of emission connecting the two main mass agglomerates in NGC 4756 suggests that hot gas links the two condensations, but we were unable to assess its full-scale distribution.

In the above framework, we considered whether the formation and/or evolution of the bright members, NGC 4756 and NGC 5328, are different or whether they have followed similar paths. In this latter case, we ask whether we can identify at which phase of their evolution we are observing them.

To address these questions, we attempted to best fit the overall SEDs and global properties of NGC 4756 and NGC 5328, selecting from a large set of chemo-photometric SPH simulations the solutions consistent with the dynamical properties of their groups (see below).

Our SPH simulations of galaxy formation and evolution start from the same initial conditions described in Mazzei & Curir (2003) and Mazzei (2003), i.e., collapsing triaxial systems initially composed of dark matter (DM) and gas in different proportions and different total masses. We then allowed a large set of galaxy encounters involving systems with a range of mass ratios from 1:1 to 1:10. In what follows, we did not consider minor mergers, since they do not represent the observed global properties that we observe today.

To exploit a vast range of orbital parameters, we carried out different simulations for each pair of interacting systems, varying the orbital initial conditions in order to have, for the ideal Keplerian orbit of two mass points, the first peri-center separation, p, ranging from the initial length of the major axis of the dark matter triaxial halo of the primary system to one-thenth of the same (major) axis.

For each of these separations, we changed the eccentricity in order to have hyperbolic orbits of different energies. For the most part, we studied direct encounters, where the spins of the systems are equal (Mazzei & Curir 2003), generally parallel to each other, and perpendicular to the orbital plane. However, we also analyzed some cases with misaligned spins in order to enhance the effects of the system initial rotation on the results. Moreover, for a given set of encounters with the same orbital parameters we also examined the role of increasing the initial gas fractions. These simulations are fully discussed elsewhere (Mazzei, in prep.).

All simulations include the self–gravity of gas, stars, and DM, radiative cooling, hydrodynamical pressure, shock heating, artificial viscosity, star formation (SF) and feedback from evolved stars and Type II SNe, and chemical enrichment. The initial mass function (IMF) is of Salpeter type with an upper mass limit of 100 $M_\odot$ and a lower mass limit of 0.01 $M_\odot$ (Salpeter 1955; see Mazzei & Curir 2003, and references therein for a discussion).

As a result, all our simulations provide us with the synthetic SED at each evolutionary step, which accounts for the chemical evolution, stellar emission, internal extinction, and re-emission by dust in a self-consistent way, as described in Spavone et al. (2009, and references therein) and extends over almost four orders of magnitude in wavelength, i.e., from 0.05 to 1000 μm. Hence, each simulation self-consistently accounts for morphological, dynamical, and chemo-photometric evolution. Additionally, we can predict the spatial distribution of clouds of hot gas ($T \geq 3 \times 10^6$ K) and total emitted power in the X-ray spectral range, computed following the prescriptions of McCray & Snow (1979).

The whole SEDs of NGC 5328 and NGC 4756 and their global properties were well-matched by two different snapshots, i.e., two different ages, of the same simulation. Each galaxy resulted from a major merger. The total initial masses of the systems were 2×10^{13} $M_\odot$ with a gas fraction 0.05, so that the total initial mass of the gas was 1×10^{12} $M_\odot$. The mass particle resolution was 5×10^7 $M_\odot$ for gas and 10^9 $M_\odot$ for DM particles, which required 40 000 initial particles.

Together with the initial masses, the orbital initial conditions adopted were: i) the first peri-center separation was 349 kpc, corresponding to one-fifth of the major axis of the primary system; ii) the orbit eccentricity was 1.3; and iii) the anomaly was 200°. Stars were born in the inner regions of their halos after about 3 Gyr from the beginning of the simulation start. Galaxies grew by changing their shapes step by step as their trajectories approached and their halos mixed.

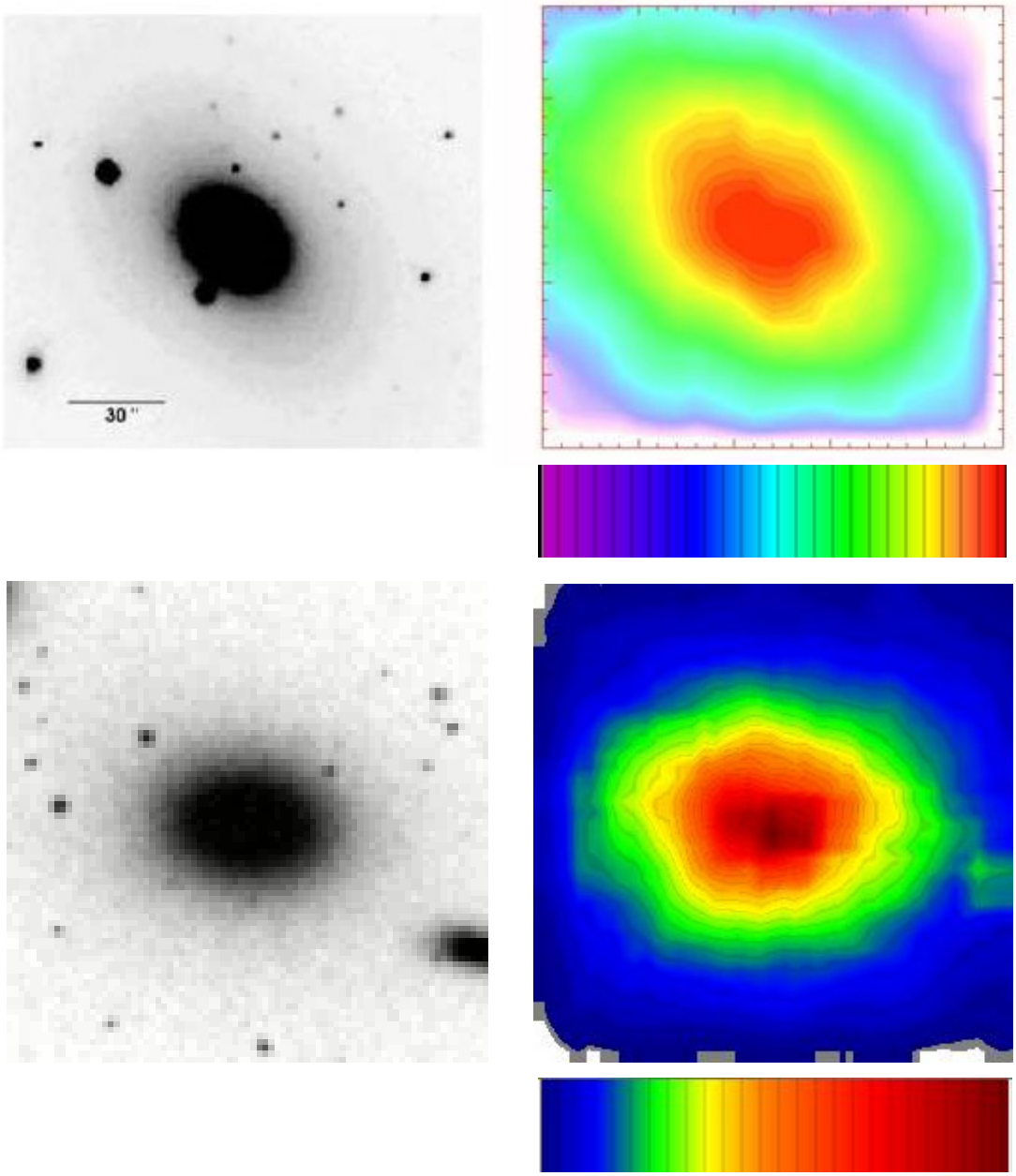

Fig. 13. *Left*: 2.5′ × 2.5′ *R*-band DSS image of NGC 4756 (*top*) and of NGC 5328 (*bottom*). *Right*: *R* map, of *YZ* projection of the selected snapshot, on the same scale as DSS image: 60 equispaced levels with density contrast equal to hundred, normalized to the total flux in the map; the *lower panel* shows the color distribution of different levels, from the maximum, red, to the minimum value, violet.

5.1. NGC 4756

A passive phase following the turn off of a star formation episode gives a good representation of the global properties of NGC 4756. The star formation was triggered 7 Gyr ago by the strong interaction between the systems involved in the major merger that produced the galaxy.

Within ∼1 $r_{\rm eff}(B)$ [∼12″, 3.6 kpc], the simulation expects a stellar population with an average age of 7.5 Gyr, and 10.5 Gyr inside ∼10$r_{\rm eff}(B)$ [36 kpc]. The *B* band absolute magnitude of the model, –21.06 mag, agrees well with the cosmologically corrected value from HyperLeda, –20.83, and the $B - R$ color, 1.76 mag, is consistent with the estimate by Grützbauch et al. (2005a), of 1.65 mag. Figure 13 compares, on the same scale 2.5′ × 2.5′, the DSS *R* band image of NGC 4756 with the *R* map of the *YZ* projection of the selected snapshot, while Fig. 14 compares the predicted SED with the available data; the far-infrared region is not strongly constrained given that only upper limits are available.

The star formation rate (SFR) of stars ≤0.05 Gyr old is 0.3 $M_\odot$ yr^{-1} and 0.7 $M_\odot$ yr^{-1} inside 2 $r_{\rm eff}(B)$ and 10 $r_{\rm eff}(B)$, respectively. The rotation velocity, weighted in terms of *V* luminosity, goes from 24 km s^{-1} at 4$r_{\rm eff}(B)$ up to 40 km s^{-1} at 15$r_{\rm eff}(B)$; the velocity dispersion in the very inner regions ($r = r_{\rm eff}/8 \simeq 0.7$ kpc) is 174 km s^{-1} in agreement with the results of ∼200 km s^{-1} by Grützbauch et al. (2005a). So this system is a slow rotator.

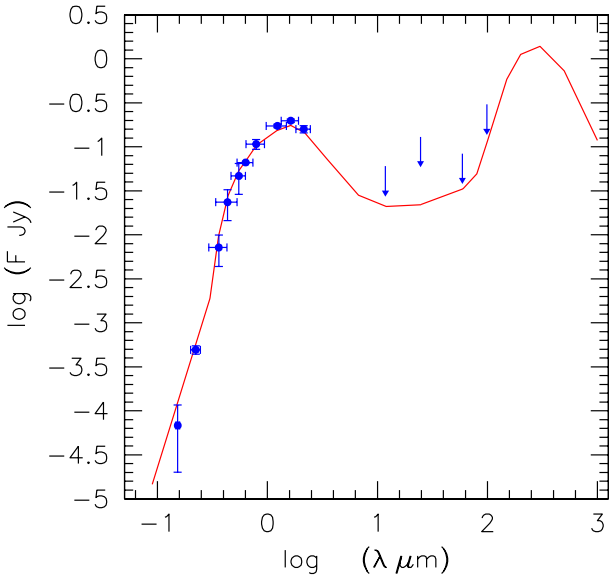

Fig. 14. Spectral energy distribution for NGC 4756: (blue) filled circles correspond to data from NED and Grützbauch et al. (2005a) in B and R bands. Arrows show upper limits; error bars indicate the band width and 3σ uncertainties. The continuous line (red) shows the predictions of our model (see text). Dust components (warm and cold with PAH, discussed in Mazzei et al. 1992) with the same average properties derived by Mazzei & De Zotti (1994) for a complete sample of nearby early-type galaxies are included (i.e. $I_0 = 46\,I_{\rm local}$, $Iw = 200\,I_{\rm local}$, $R_{\rm wc} = 0.27$ and $r_{\rm d} = 100\,r_{\rm c}$, see in Mazzei et al. 1994).

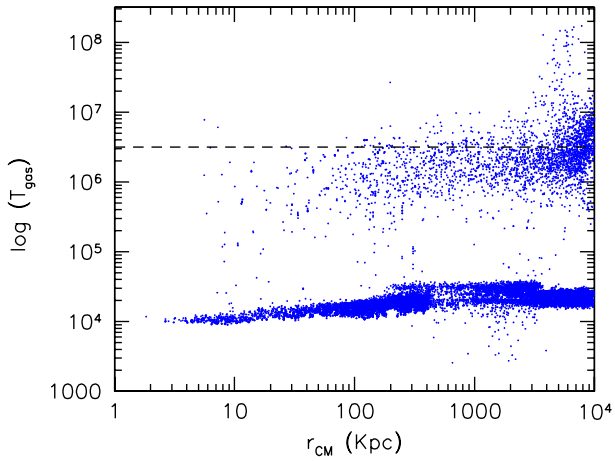

Fig. 15. Radial distribution of the temperature of gas clouds in a frame corresponding to the galaxy center of mass weighted by V luminosity. Each point indicates the simulated gas clouds at the given temperature.

The simulations also provide an estimate of the mass and the X-ray luminosity of the system at the time of the snapshot.

The total mass expected from our simulation within 157 kpc, which corresponds to the virial radius of the group (where $R_{\rm vir} = \pi/2 \times R_{\rm H} = 1.57\ R_{\rm H}$, with the harmonic radius $R_{\rm H}$ from Table 1), is $M_{\rm T} \sim 3.73 \times 10^{12}\ M_{\odot}$. Close to 90% of this mass is in the form of a dark matter halo, since the stellar contribution is $\sim 3 \times 10^{11}\ M_{\odot}$. This value is well below the virial mass given in Table 1, based on the dynamical analysis of the group.

This can be understood if the simulation is able to explain the formation and evolution of the brightest member for which the SED, total stellar luminosity, and internal dynamics are well-matched by the simulation, but does not exactly reproduce the distribution of the mass, which is on a larger scale than indicated by the dynamical analysis. The discrepancy in mass could also indicate that the assumption that the group is well-virialized is not entirely correct on this scale. The estimate of the virial radius is relatively unstable, and the inclusion or exclusion of a few members modifies it significantly with smaller variations in the virial mass (see Table 1). For example, the simulated and "measured" mass within a virial radius of 300 kpc, obtained by ignoring the SW sub-clump in the dynamical analysis, are in significantly better agreement, 1 vs. $2.9 \times 10^{13}\ M_{\odot}$. This is also consistent with the dynamical evidence that the projected mass is higher than the derived virial mass (see Sect. 2).

The spatial distributions of the hot gas at the selected snapshot is shown in Fig. 15. In this figure, the reference frame corresponds to the center of mass of the galaxy. The total luminosity in the X ray spectral range due to gas at $T \geq 3 \times 10^6$ K is $L_{\rm x} = 1.7 \times 10^{41}$ erg/s inside 40 kpc, in agreement with the values measured with *XMM-Newton*.

5.2. NGC 5328

To get a good fit to the global properties of NGC 5328, the simulation needs to be stopped at a time corresponding to an age of 2.25 Gyr younger than NGC 4756, so that the last episode of star formation ended about 4.5 Gyr ago.

The average population age inside $1 r_{\rm eff}(B)$ [$\sim$53″ or 17 kpc] is 7 Gyr, and 9 Gyr inside $\sim 3 r_{\rm eff}(B)$ [$\sim$50 kpc]. We note that $r_{\rm eff}(B)$ is about five times larger than that of NGC 4756 (Grützbauch et al. 2005a), therefore the regions probed are significantly different in the two objects, which results in similar average ages for the stars. Annibali et al. (2007) provided a luminosity weighted age of 12.7 ± 3.4 Gyr for the nuclear region modeling line-strength indices, hence even considering the large error, NGC 5328 is an old object. Weak emission lines from warm gas are present in the nuclear region of NGC 5328. The perturbation induced in the measure of the line strength has been taken into account in the Annibali et al. (2007) measures. Continuing their study, Annibali et al. (2010) analyzed the powering mechanism of the warm gas. They found that the activity class of NGC 5328 nucleus is "composite" i.e. it lies in-between pure star-forming galaxies and LINERs. Both observations and our simulation suggest that NGC 5328 is a complex object that could have had an episode of star formation at intermediate age.

The rotation velocity, weighted in terms of V luminosity, ranges from 22 km s^{-1} to 40 km s^{-1} [$1 r_{\rm eff}(B)$ – $3 r_{\rm eff}(B)$]. Moreover, the velocity dispersion inside 2 kpc, corresponding to $r_{\rm eff}(B)/8$, is 276 km s^{-1}, in agreement with the observations (Grützbauch et al. 2005b). According to our results, this galaxy is therefore a slow rotator like NGC 4756. The B band absolute magnitude of the model, –21.22 mag, is consistent with the cosmologically corrected value from HyperLeda, –21.76, and the $B-R$ color, 1.80 mag, with the value of 1.79 mag by Grützbauch et al. (2005b).

The total mass expected within $1\ r_{\rm eff}(B)$ is $3.75 \times 10^{11}\ M_{\odot}$, with $\sim$26% consisting of dark matter. Figure 13 compares the DSS R band image of NGC 5328 with the R map of the YZ projection of the selected snapshot, and Fig. 16 the predicted SED with the available data (see Fig. 14 for details).

The predictions of this snapshot are consistent with the dynamical analysis of the group itself (Sect. 2 and Table 1). The total mass expected within 157 kpc, i.e., the virial radius of the group, $3.73 \times 10^{12}\ M_{\odot}$, agrees with the virial mass of the group

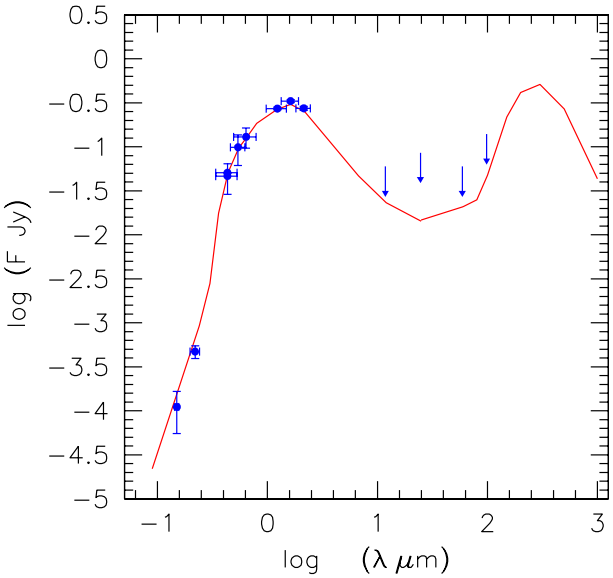

Fig. 16. Spectral energy distribution for NGC 5328, as in Fig. 14: data from NED and Grützbauch et al. (2005b) in *B* and *R* bands (blue filled circles), IR (Arrows for upper limits), and model prediction (red continuous line).

itself. Similarly, the total luminosity is $L_x = 2.91 \times 10^{41}$ erg/s inside 110 kpc, which is consistent with the values measured from the *XMM-Newton* data.

6. Summary and conclusions

We have detected both NGC 4756 and NGC 5328 with *XMM-Newton* data, and measured a sizable contribution from the hot gas in both systems. In both galaxies, the extent of the X-ray emission is larger than their optical size. For NGC 5328, we have measured a total size of ∼110 kpc. NGC 4756 is projected against an X-ray emitting background cluster, which prevented us from properly measuring the total extent of the source. However, we have detected emission out to a radius of ∼40 kpc around NGC 4756, and a connection to the SW compact-like group at ∼130 kpc, which is presumably interacting with NGC 4756 itself. The total luminosities measured are $L_x \sim 10^{41}$ erg s^{-1}, which is relatively low for groups but should be considered a lower limit for NGC 4756.

The results of our SPH simulations, which describe the dynamical, morphological, and chemo-photometric evolution in a self-consistent way, suggest that NGC 4756 and NGC 5328 can be described by the same evolutionary path, which were stopped at two different epochs, with the last episode of star formation occurring at 7 Gyr and 4.5 Gyr ago, respectively. The data and simulations describe old and digested merging events as the origin of both galaxies, which can now be considered mature systems. The predictions are in good agreement with observed quantities such as the SED, σ for stars, and X-ray luminosity.

In spite of the apparent similarity of these two galaxies, in terms of luminosity, internal rotation, stellar content, and evolutionary path, our evidence suggests that their respective groups are at different evolutionary phases.

A new analysis of the dynamics of both systems has confirmed that NGC 5328 sits at the center of a small group, which appears to be azimuthally symmetric and relatively relaxed. NGC 5328 is the dominant galaxy in the system, about 2 mag. brighter than the next brightest object. The group has a relatively low virial mass, of a few $\sim 10^{12}$ $M_\odot$, comparable to what is expected for a bright early-type galaxy. The presence of Abell 3574 at the same redshift suggests that this could be a satellite galaxy at the very periphery of the much larger cluster potential, that has gone through major preprocessing before being [eventually] acquired by the cluster.

NGC 4756 is composed of two main sub-condensations, NGC 4756 itself and a compact-like small group. The two are at the same average redshift, but might not yet have reached dynamical equilibrium. The evidence of a connection in the X-ray emission between the two condensations suggests that there is an interaction between the two structures that might eventually merge at a later stage of the group evolution.

Acknowledgements. We wish to thank the EPIC blank sky team, Jenny Carter and Andy Read, for the effort they put into helping us solve our background issues and the clever suggestions that they made. We thank Giovanni Fasano for having kindly provided us with a *V*-band image of Abell 1361 observed at ESO-MPI2.2 m with WFI as part of the WINGS project. We acknowledge a financial contribution from the agreement ASI-INAF I/009/10/0. This research has made use of the SAOImage DS9, developed by Smithsonian Astrophysical Observatory and of the NASA/IPAC Extragalactic Database (NED) which is operated by the Jet Propulsion Laboratory, California Institute of Technology, under contract with the National Aeronautics and Space Administration. IRAF is distributed by the National Optical Astronomy Observatories, which are operated by the Association of Universities for Research in Astronomy, Inc., under cooperative agreement with the National Science Foundation. The Digitized Sky Survey (DSS) was produced at the Space Telescope Science Institute under US Government grant NAG W-2166. The images of these surveys are based on photographic data obtained using the Oschin Schmidt Telescope at the Palomar Observatory and the UK Schmidt Telescope. The plates were processed into the present compressed digital form with the permission of these institutions. We acknowledge the usage of the HyperLeda database (http://leda.univ-lyon1.fr).

References

Aceves, H., & Perea, J. 1999, A&A, 345, 439
Anders, E., & Grevesse, N. 1989, Geochim. Cosmochim. Acta, 53, 197
Annibali, F., Bressan, A., Rampazzo, R., Zeilinger, W. W., & Danese, L. 2007, A&A, 463, 455
Annibali, F., Bressan, A., Rampazzo, R., et al. 2010, A&A, 519, A40
Annibali, F., Grützbauch, R., Rampazzo, R., Bressan, A., & Zeilinger, W. W. 2011, A&A, 528, A19
Baade, D., Meisenheimer, K., Iwert, O., et al. 1999, The Messenger, 95, 15
Bai, L., Rasmussen, J., Mulchaey, J. S., et al. 2010, ApJ, 713, 637
Baldi, A., Forman, W., Jones, C., et al. 2009, ApJ, 694, 479
Bettoni, D., Galletta, G., Rampazzo, R., et al. 2011, A&A, 534, 24
Bettoni, D., Buson, L, Mazzei, P., & Galleta, G., 2012, MNRAS, accepted [arXiv:1204.3472]
Berrier, J. C., Stewart, K. R., Bullock, J. S., et al. 2009, ApJ, 690, 1292
Boroson, B., Kim, D.-W., & Fabbiano, G. 2011, ApJ, 729, 12
Carter, J. A., & Read, A. M. 2007, A&A, 464, 1155
Coziol, R., Iovino, A., & de Carvalho, R. R. 2000, AJ, 120, 47
Eke, V. R., Baugh, C. M., Cole, S., Frenk, C. S., & Norberg, P. 2004, MNRAS, 348, 866
Feldmann, R., Carollo, C. M., Mayer, L., et al. 2010, ApJ, 709, 218
Feldmann, R., Carollo, C. M., & Mayer, L. 2011, ApJ, 736, 88
Fergusson, H. C., & Sandage, A. 1990, AJ, 100, 1
Firth, P., Evstigneeva, E. A., Jones, J. B., et al. 2006, MNRAS, 372, 1856
Fruscione, A., Mc Dowell, J. C., Allen, G. E., et al. 2006, Proc. SPIE, 6270, 60
Garcia, A. M. 1993, A&AS, 100, 47
Giuricin, G., Marinoni, C., Ceriani, L., & Pisani, A. 2000, ApJ, 543, 178
Grevesse, N., & Sauval, A. J. 1998, Space Sci. Rev., 85, 161
Grützbauch, R., Klem, B., Focardi, P., et al. 2005a, AJ, 129, 1848
Grützbauch, R., Annibali, F., Bressan, A., et al. 2005b, MNRAS, 364, 146
Grützbauch, R., Zeilinger, W. W., Rampazzo, R., et al. 2009, A&A, 502, 473
Heisler, J., Tremaine, S., & Bahcall, J. N. 1985, ApJ, 298, 8
Jeltema, T. E., Binder, B., & Mulchaey, J. S. 2008, ApJ, 679, 1162
Kalberla, P. M. W., Burton, W. B., Hartmann, D., et al. 2005, A&A, 440, 775
Kawata, D., & Mulchaey, J. S. 2008, ApJ, 672, L103
Kim, D.-W., Kim, E., Fabbiano, G., & Trinchieri, G. 2008, ApJ, 688, 931
Kobayashi, C. 2005, MNRAS, 361, 1216

Kovaĉ, K., Lilly, S. J., Knobel, C., et al. 2010, ApJ, 718, 86
Mahdavi, A., & Geller, M. J. 2001, ApJ, 554, 129
Marino, A., Iodice, E., Tantalo, R., et al. 2009, A&A, 508, 1235
Marino, A., Bianchi, L., Rampazzo, R., Buson, L. M., & Bettoni, D. 2010, A&A, 511, A29
Marino, A., Plana, H., Rampazzo, R., et al. 2012, MNRAS, submitted
Mathews, W. G. 1990, ApJ, 354, 468
Mathews, W. G., & Brighenti, F. 2003, ARA&A, 41, 191
Mazzei, P. 2003, Mem. SAIT, 74, 498
Mazzei, P., & Curir, A. 2003, ApJ, 591, 784 (MC03)
Mazzei, P., & De Zotti, G. 1994, ApJ, 426, 97
Mazzei, P., Xu, G., & De Zotti, G. 1992, A&A, 256, 45
Mazzei, P., De Zotti, G., & Xu, G. 1994, ApJ, 422, 81
McCray, R., & Snow, T. 1979, ARA&A, 17, 213
Mulchaey, J. S. 2000, ARA&A, 38, 289
Mulchaey, J. S., Davis, D. S., Mushotzky, R. F., & Burstein, D. 2003, ApJS, 145, 39
O' Sullivan, E., Worrall, D. M., Birkinshaw, M., et al. 2011, MNRAS, 416, 2916
Panuzzo P., Rampazzo, R., Bressan, A., et al. 2011, A&A, 528, 10
Peng, Y., Lilly, S. J., Kovaĉ, K., et al. 2010, ApJ, 721, 193
Perez, J., Tissera, P., Padilla, N., Alonso, M. S., & Lambas, D. G. 2009, MNRAS, 399, 1157
Rampazzo, R., Annibali, F., Bressan, A., et al. 2005, A&A, 433, 497
Salpeter, E., & Edwin, E. 1955, ApJ, 121, 161
Spavone, M., Iodice, E., Calvi, R., et al. 2009, MNRAS, 393, 317
Tago, E., Einasto, J., Saar, E., et al. 2008, A&A, 479, 927
Takizawa, M., Nagino, R., & Matsushita, K. 2010, PASJ, 62, 951
Tully, B. 2011, EAS Pub. Ser., 48, 281

Pages 17 to 19 are available in the electronic edition of the journal at http://www.aanda.org

Appendix A: Detected sources in the fields of NGC 4756 and NGC 5328

Besides the two galaxies themselves, the detection algorithm detected 68 and 32 sources in the fields of NGC 4756 and NGC 5328, respectively. For the latter galaxy field, we have excluded a region of 1′ radius around NGC 5328, where the sources detected most likely represent merely small fluctuations in the extended emission. We used a broad energy band 0.5–4.5 keV and a single conversion factor to convert the detected counts into flux, corresponding to a power-law model with $\Gamma = 1.7$ and $N_{\rm H} = 3\times10^{20}$ cm^{-2} (see 2XMM catalog). In Tables A.1 and A.2 we give the full list of detected sources, excluding NGC 4756 and NGC 5328 themselves (see Table 2). We give the counts and average flux derived from the three instruments combined, when available. For sources detected in only a subset of the instruments, we give the counts and fluxes from the specific instrument, as noted in the tables. Identifications with optical objects is given when available, or a comment is provided when the positional coincidence indicates a clear association.

Table A.1. Detected sources in the field of NGC 4756.

Nr.	α (J2000.0)	δ (J2000.0)	Counts 0.5–4.5 keV	Error	f_x (0.5–4.5 keV) erg cm^{-2} s^{-1}	Identification
1	12:51:49.623	–15:32:21.25	271.3	20.4	3.3×10^{-14}	Background galaxy
2	12:51:52.791	–15:29:36.60	119.4	16.0	1.3×10^{-14}	
3	12:51:53.713	–15:24:47.18	65.9	12.5	7.9×10^{-15}	Faint object
4	12:51:54.418	–15:33:10.47	85.5	14.0	8.8×10^{-15}	
5†	12:51:55.915	–15:18:48.28	38.5	9.2	1.1×10^{-14}	
6	12:52:01.404	–15:34:29.50	342.6	22.5	3.4×10^{-14}	
7	12:52:01.580	–15:22:28.62	96.8	14.6	8.7×10^{-15}	
8	12:52:03.609	–15:39:31.34	49.9	11.2	2.7×10^{-15}	Point-like source?
9	12:52:03.881	–15:39:04.38	129.8	16.4	1.6×10^{-14}	
10	12:52:04.073	–15:27:33.42	54.3	13.2	4.1×10^{-15}	Next to bright!
11	12:52:04.147	–15:35:58.62	108.0	15.2	1.0×10^{-14}	
12	12:52:04.161	–15:27:09.39	99.5	15.6	7.5×10^{-15}	
13	12:52:04.622	–15:23:57.42	368.2	23.8	3.0×10^{-14}	Faint object
14	12:52:06.664	–15:35:54.55	73.9	13.8	6.3×10^{-15}	
15	12:52:07.715	–15:26:17.79	445.9	26.1	3.3×10^{-14}	Faint object
16	12:52:10.984	–15:20:16.18	49.7	12.1	3.8×10^{-15}	
17	12:52:11.796	–15:24:38.70	156.5	17.9	1.0×10^{-14}	
18	12:52:11.822	–15:19:11.73	228.6	25.1	2.1×10^{-14}	
19	12:52:14.795	–15:34:23.98	192.1	19.0	1.5×10^{-14}	USGC S188
20	12:52:15.048	–15:23:47.64	76.8	13.7	5.1×10^{-15}	
21	12:52:15.998	–15:17:05.75	76.9	14.7	8.5×10^{-15}	
22	12:52:18.912	–15:21:47.07	122.1	19.5	1.2×10^{-14}	At the border of a bright object
23	12:52:19.527	–15:41:24.46	222.0	40.9	2.8×10^{-14}	
24	12:52:23.679	–15:22:50.09	112.0	15.8	6.3×10^{-15}	Bright point-like source
25	12:52:23.760	–15:30:12.39	142.6	18.0	9.4×10^{-15}	
26	12:52:24.129	–15:33:27.32	83.6	14.4	5.2×10^{-15}	
27	12:52:25.149	–15:32:16.74	136.6	17.2	7.4×10^{-15}	Background galaxy at $z = 0.151461$
28	12:52:27.148	–15:31:05.81	470.4	43.1	2.6×10^{-14}	IC 0829
29	12:52:28.301	–15:32:24.75	73.1	17.0	3.4×10^{-15}	
30	12:52:29.912	–15:34:32.16	131.9	18.3	9.1×10^{-15}	
31	12:52:31.041	–15:30:37.22	61.0	15.0	2.4×10^{-15}	
32†	12:52:31.334	–15:17:18.18	169.9	16.3	3.4×10^{-14}	Faint object
33	12:52:31.424	–15:40:32.81	89.9	14.8	9.1×10^{-15}	
34	12:52:32.113	–15:39:43.08	56.5	13.2	3.8×10^{-15}	Point-like source?
35	12:52:32.157	–15:28:52.90	266.2	28.7	1.3×10^{-14}	
36	12:52:32.405	–15:28:41.90	997.9	42.8	5.4×10^{-14}	Background point-like source?
37	12:52:33.154	–15:30:59.84	2111.0	52.2	1.0×10^{-13}	MCG-02-33-038
38†	12:52:36.126	–15:18:20.10	78.1	12.5	1.4×10^{-14}	Galaxy in A1361
39	12:52:37.950	–15:31:51.01	237.8	21.3	1.1×10^{-14}	Faint object
40	12:52:39.329	–15:34:57.21	43.3	12.5	3.3×10^{-15}	Point-like source
41	12:52:40.258	–15:41:22.77	75.8	15.5	5.6×10^{-15}	
42	12:52:40.777	–15:32:04.98	59.9	13.4	2.6×10^{-15}	Galaxy in A1361
43	12:52:41.277	–15:26:04.90	443.1	27.7	1.9×10^{-14}	
44	12:52:43.931	–15:35:20.65	106.8	18.0	7.1×10^{-15}	

Table A.1. continued.

Nr.	α (J2000.0)	δ (J2000.0)	Counts 0.5–4.5 keV	Error	f_x (0.5–4.5 keV) erg cm^{-2} s^{-1}	Identification
45	12:52:44.296	–15:40:25.71	42.0	11.0	1.0×10^{-15}	Point-like source?
46	12:52:45.037	–15:28:32.55	239.5	22.0	1.0×10^{-14}	
47	12:52:45.619	–15:25:19.94	417.0	27.9	1.9×10^{-14}	Background point-like source?
48	12:52:48.390	–15:26:26.97	491.8	30.0	2.2×10^{-14}	
49[†]	12:52:50.291	–15:22:15.60	71.8	13.2	9.1×10^{-15}	
50[†]	12:52:50.385	–15:19:38.71	155.2	16.5	2.5×10^{-14}	Faint object
51	12:52:50.469	–15:24:04.39	915.6	104.1	5.0×10^{-14}	Point-like source in halo of NGC 4756
52	12:52:52.749	–15:35:44.31	135.0	17.7	9.2×10^{-15}	
53	12:52:54.319	–15:41:31.59	780.6	85.9	8.1×10^{-15}	
54[†]	12:52:56.058	–15:20:30.42	86.1	14.5	1.4×10^{-14}	Galaxy in A1361
55[†]	12:52:57.588	–15:20:44.61	56.7	12.6	8.9×10^{-15}	Galaxy in A1361
56	12:52:58.104	–15:34:51.93	104.9	16.9	8.1×10^{-15}	
57	12:53:01.051	–15:39:38.33	472.4	27.3	4.8×10^{-14}	Faint object
58[†]	12:53:02.525	–15:21:22.32	56.3	11.7	9.5×10^{-15}	
59	12:53:05.937	–15:39:11.63	102.0	16.3	1.0×10^{-14}	
60	12:53:08.930	–15:34:21.28	92.5	15.1	6.4×10^{-15}	
61	12:53:10.535	–15:26:24.85	179.7	18.9	1.2×10^{-14}	
62[†]	12:53:11.936	–15:21:16.02	40.5	10.7	7.4×10^{-15}	
63	12:53:18.411	–15:32:04.01	2226.1	63.7	1.8×10^{-13}	Galaxy in A1361
64	12:53:20.118	–15:25:40.59	106.2	16.7	8.2×10^{-15}	Bright object
65	12:53:25.348	–15:28:09.22	270.4	22.0	2.6×10^{-14}	Background galaxy
66[††]	12:53:26.011	–15:33:30.90	45.2	10.3	1.6×10^{-14}	
67[†††]	12:53:30.483	–15:22:31.08	32.3	8.7	1.2×10^{-14}	
68[†††]	12:53:32.550	–15:32:03.40	32.8	9.0	1.2×10^{-14}	

Notes. [(†)] EPIC-pn data. [(††)] EPIC-M1 data. [(†††)] EPIC-M2 data.

Table A.2. Detected sources in the field of NGC 5328.

Nr.	α (J2000.0)	δ (J2000.0)	Counts 0.5–4.5 keV	Error	f_x (0.5–4.5 keV) erg cm^{-2} s^{-1}	Identification
1[†]	13:51:52.001	–28:27:27.35	87.7	20.2	5.0×10^{-14}	2MASXJ13515205-2827344 z = 0.037336
2	13:52:00.238	–28:25:34.53	53.9	13.0	1.8×10^{-14}	
3	13:52:10.571	–28:25:05.76	20.6	7.9	1.9×10^{-15}	
4	13:52:16.906	–28:30:41.24	24.1	8.3	2.3×10^{-15}	
5	13:52:18.030	–28:27:46.10	85.2	14.6	1.9×10^{-14}	
6	13:52:20.045	–28:38:16.72	63.3	13.2	1.9×10^{-14}	
7	13:52:20.886	–28:33:59.91	46.2	12.1	8.3×10^{-15}	
8[†]	13:52:22.080	–28:31:17.68	86.4	15.3	2.5×10^{-14}	Faint object
9	13:52:26.736	–28:22:22.45	148.2	17.1	3.1×10^{-14}	Faint object
10	13:52:26.870	–28:31:53.59	265.8	21.3	4.8×10^{-14}	Point source
11[††]	13:52:27.550	–28:41:53.07	30.1	7.3	3.6×10^{-14}	Bright object (star?)
12	13:52:33.988	–28:28:50.22	47.1	12.2	4.7×10^{-15}	
13	13:52:38.310	–28:15:58.81	45.1	12.3	1.3×10^{-14}	Star
14	13:52:39.980	–28:18:03.54	77.3	14.2	2.0×10^{-14}	
15	13:52:44.040	–28:23:56.25	200.2	19.0	3.0×10^{-14}	
16	13:52:48.781	–28:29:59.46	517.1	115.7	6.7×10^{-14}	PGC3094716
17	13:52:49.010	–28:35:31.03	84.3	13.9	1.4×10^{-14}	
18	13:52:49.283	–28:28:10.60	60.2	15.0	6.0×10^{-15}	
19[†]	13:52:50.496	–28:17:47.37	52.6	11.9	1.8×10^{-14}	
20	13:52:53.884	–28:31:46.93	70.1	14.7	8.0×10^{-15}	2MASXJ13525393-2831421
21	13:52:54.091	–28:30:35.46	604.1	52.5	9.1×10^{-14}	
22	13:52:57.238	–28:28:01.18	63.8	15.3	7.0×10^{-15}	
23	13:52:59.138	–28:28:21.73	221.4	38.4	2.5×10^{-14}	NGC 5330
24	13:52:59.887	–28:35:23.05	150.4	17.2	2.4×10^{-14}	CXO J135259.8-283523, bright object
25	13:53:02.056	–28:40:44.45	110.1	15.4	2.8×10^{-14}	
26[†††]	13:53:03.219	–28:14:52.84	103.8	11.6	2.1×10^{-13}	CXO J135303.0-281502
27	13:53:08.095	–28:34:05.41	93.6	14.8	1.1×10^{-14}	
28	13:53:14.928	–28:25:40.86	49.6	13.6	1.2×10^{-14}	ESO445-070
29[†]	13:53:27.950	–28:23:02.20	303.3	21.6	7.6×10^{-14}	Faint object
30	13:53:31.424	–28:34:07.20	47.1	11.8	9.2×10^{-15}	
31[††]	13:53:40.261	–28:35:55.30	34.7	8.1	2.4×10^{-14}	
32[††]	13:53:52.645	–28:29:07.54	25.4	7.0	2.3×10^{-14}	

Notes. [(†)] EPIC-pn data. [(††)] EPIC-M1 + EPIC-M2 data. [(†††)] EPIC-M2 data.